POLITECNICO DI TORINO
Repository ISTITUZIONALE

A node-based version of the cellular Potts model

Original
A node-based version of the cellular Potts model / Scianna, Marco; Preziosi, Luigi. - In: COMPUTERS IN BIOLOGY AND MEDICINE. - ISSN 0010-4825. - 76:(2016), pp. 94-112. [10.1016/j.compbiomed.2016.06.027]

Availability:
This version is available at: 11583/2649595 since: 2020-02-18T22:21:57Z

Publisher:
Elsevier Ltd

Published
DOI:10.1016/j.compbiomed.2016.06.027

Terms of use:

This article is made available under terms and conditions as specified in the corresponding bibliographic description in the repository

Publisher copyright
Elsevier postprint/Author's Accepted Manuscript

© 2016. This manuscript version is made available under the CC-BY-NC-ND 4.0 license http://creativecommons.org/licenses/by-nc-nd/4.0/.The final authenticated version is available online at: http://dx.doi.org/10.1016/j.compbiomed.2016.06.027

(Article begins on next page)

09 April 2024

A node-based version of the cellular Potts model

Marco Scianna[1] and Luigi Preziosi[2]

Department of Mathematical Sciences, Politecnico di Torino, Corso Duca degli Abruzzi 24, 10129 Torino, Italy

---

Abstract

The cellular Potts model (CPM) is a lattice-based Monte Carlo method, that uses an energetic formalism to describe the phenomenological mechanisms underlying the biophysical problem of interest. We here propose a CPM-derived framework, that relies on a node-based representation of cell-scale elements. This feature has relevant consequences on the overall simulation environment. First, our model can be implemented on any given domain, provided a proper discretization (which can be regular or irregular, fixed or time evolving). Then, it is allowed an explicit representation of cell membranes, whose displacements realistically result in cell movement. Finally, our node-based approach can be easily interfaced with continuous mechanics or fluid dynamics models. The proposed computational environment is here applied to some simple biological phenomena, such as cell sorting and chemotactic migration, also in order to achieve an analysis of the performance of the underlying algorithm. This work is finally equipped with a critical comparison between the advantages and disadvantages of our model with respect to the traditional CPM and to some similar vertex-based approaches.

Keywords: cellular Potts model, multiscale model, cell surface rearrangement, cell membrane node, domain discretization

---

1. Introduction and motivation

The evolution of biological systems is determined by mechanisms and processes operating at different spatiotemporal scales, i.e., from the microscopic/molecular level to the macroscopic/multicellular level. Each scale

---

[1] E-Mail: `marcosci1@alice.it`

[2] E-Mail: `luigi.preziosi@polito.it`

can be properly approached with selected mathematical methods. In this respect, individual cell-based models (IBMs) are particularly suitable to describe mesoscopic cell-level dynamics. They in fact allow to preserve the identity of the single component individuals of the system and to capture their behavior and mutual interactions. This family of theoretical approaches can be then classify according to the type of representation given to each cell, which may consist in a material point, an undeformable sphere or ellipsoid or in a deformable polygon or subset of domain elements.

One of the well-known IBMs is the cellular Potts model (CPM, also called the Glazier-Graner-Hogeweg model, see [40, 43] and [41, 42, 64, 93] for reviews). The CPM is a grid-based Monte Carlo method, which implements an energy minimization principle to determine the evolution of the simulated system. All CPMs are based on regular numerical lattices as domains, and define a list of discrete objects. They are spatially-extended cell-scale elements, which consist of patches of lattice sites sharing the same (integer) identification number. Continuous fields can be included in the modeling environment as well, conferring the CPM a multiscale-hybrid nature. They represent the spatio-temporal evolution of microscopic quantities, such as diffusive ions and molecules. Attributes of discrete individuals and rules for their dynamics and for their interactions with selected fields are described by an effective potential formalism, which results in a system energy given by a *Hamiltonian*. This functional describes indeed the state of the system, whose rearrangements are driven by an algorithm of stochastic minimization, i.e., an iterative Metropolis procedure which accounts for a probabilistic acceptance of random updates of lattice configurations. As long as a biological mechanism can be described with an energetic formalism, it can be included in the CPM framework. In this respect, the CPM is not specific for a given type of biological problems, but it can be rather considered as a framework for model building. For these reasons, the CPM method is becoming an increasingly common technique for the mathematical modeling of a wide range of phenomena.

In this foundational work, we present a new version of the CPM, which is still based on an energy minimization philosophy, but which relies on a vertex-based representation of the discrete cell-scale objects. Besides its intrinsic novelty, our approach has some advantages from a modeling point of view. For instance, it can be employed on every given physical domain (provided a proper discretization): this may be useful for a computational coupling with selected continuum mechanics or fluid dynamics models. Our approach then allows to explicitly represent cell membrane, with its extended protrusions (e.g., filopodia, pseudopodia), and to avoid the introduction of a generalized medium element when it is not necessary. Such main model features will be presented in Section 2. In particular, we will describe the Metropolis algorithm underlying our approach and propose some possible Hamiltonians, that can be implemented in the resulting computational framework. We will further indicate some procedures to implement more complex cell dynamics (i.e., division, compartmentalization). Section 3 will be instead focused on sample applications, dealing with single cell and multicellular dynamics. Such simulation outcomes will allow also to achieve a qualitative relationship between variations in some relevant model parameters and the resulting system evolution. An analysis of the computational efficiency of our method, compared with the traditional version of the CPM, will be instead provided in Section 4. This work will be finally equipped by a detailed discussion, where the advantages and the disadvantages of the proposed model with respect both to classical CPM approaches and to similar vertex-based models will be commented.

2. Proposed mathematical model

As traditional Potts models, our approach includes both discrete cell-scale elements and continuous fields, while the evolution of the system comes from an iterative and stochastic minimization of its free energy.

The domain of our method can be any physical region $\Omega \subset \mathbb{R}^2$, equipped by a proper discretization, that can be regular (e.g., in the case of triangular or square grid elements) or irregular (e.g., in the case of Voronoi tessellations), fixed or adaptative according to the system dynamics (see Fig. 1 (A)). This is the first relevant difference with respect to classical CPMs which can be only employed on rigid lattices formed by equivalent (square or hexagonal) sites. Let us then define with

$$\overline{\Omega} = \left\{ \mathbf{x}_j \in \mathbb{R}^2 : j = 1, \ldots, J \right\} \tag{1}$$

the set of the spatial locations of the vertices of the domain discretization, where the integers $j = 1, \ldots, J$ their tracking numbers. The first-nearer neighborhood of a given mesh vertex j is then identified with

$$\overline{\Omega}_j = \left\{ \mathbf{x}_k \in \overline{\Omega} : k \neq j \text{ and } k \text{ belongs to the same grid element as } j \right\}, \tag{2}$$

as represented in Fig. 1 (B).

We then consider a system formed by N_c cells (or cell-scale elements). Each cell $c = 1, \dots, N_c$ is assumed to be defined by a given set of *numerically ordered* membrane nodes i, where $i = 1, \dots, V_c$ (V_c indicates the total number of nodes characterizing the c-th individual). $\mathbf{x}_{c,i}(t)$ then indicates the actual location within the domain of node i of cell c. In this respect, if, for instance, the node $i = 9$ of the cell $c = 3$ coincides, at a given time step t, with the grid vertex $j = 23$, we can write $\mathbf{x}_{3,9}(t) = \mathbf{x}_{23}$. Indeed, each cell c is defined, at a given time step t, by the following subdomain:

$$\overline{\Omega}^c(t) = \left\{ \mathbf{x}_j \in \overline{\Omega} : \mathbf{x}_j = \mathbf{x}_{c,i}(t), \text{ with } i = 1, \dots, V_c \right\}. \tag{3}$$

Remark. For the sake of clarity, we underline that the term “vertex” is used to indicate the junctions between domain grid elements. The term “node” instead denotes the punctual “hotspots” that identify each cell and that might be thought also as clusters of adhesive molecules, as we will see in the following.

The membrane of a cell c can be defined, in general, by any close unknotted curve connecting *in the right order* the component nodes of the individual (this is the reason why they need to be numerically ordered). However, for the sake of simplicity, we hereafter opt to assume that the membrane of each cell is identified by the polygonal line formed by the segments connecting two *consecutive* vertices, say i and $i + 1$. In this respect, the length of the plasma membrane of an individual c can be properly calculated as the sum of the Euclidean distances between the locations of two consecutive nodes, i.e.,

$$l_c^{\text{perimeter}}(t) = \sum_{i=1}^{V_c} |\mathbf{x}_{c,i+1}(t) - \mathbf{x}_{c,i}(t)|, \tag{4}$$

with $\mathbf{x}_{c,V_c+1}(t) = \mathbf{x}_{c,1}(t)$, for any given time t. Consistently with our hypothesis, the surface of a cell c, i.e., s_c^{surface}, can be defined as the area within the polygonal line itself. Each individual c is finally characterized by an associated type $\tau(c)$ (e.g., endothelial cell, fibroblast, ECM fiber, ...). A sample representation of a pair of cells, c and c', is given in Fig. 1 (A).

Each cell can be defined by a different number of membrane nodes and it is not necessary that they are initially equally-spaced. In this respect, they can be distributed according to the characteristic shape of the individual itself, for example applying proper post-processing techniques to selected experimental images. For instance, in the case of Fig. 1 (C), the set of cell membrane nodes is determined, and initially located, according to the following procedure: (i) the plasma membrane of the experimental cell is approximated by a close (parametrized) curve in $\mathbb{R}^2$; (ii) the points of the curve characterized by the maximal (or the minimal) curvature are selected, and reported on the computational domain $\Omega \subset \mathbb{R}^2$; (iii) the membrane nodes of the model cell are placed in grid vertices as close as possible to the reported points. From Fig. 1 (C), it also possible to observe that the proposed cell representation allows to realistically described extended membrane protrusions, such as long and thin filopodia. The number of membrane nodes characterizing a cell element can also vary in time (i.e., for a cell c, one can have that $i = 1, ..., V_c(t)$). In particular, if a node i of cell c is removed, then the remaining consecutive nodes $i-1$ and $i+1$ should be linked to avoid membrane breakage (see Fig. 2 (A), middle panels). Conversely, if a node $V_c + 1$ is added to cell c, it should be linked to the nearest pair of consecutive ones, say with i and $i+1$ (see Fig. 2 (A), top panels). Both membrane node creation and destruction require renumbering of the entire set of nodes of the interested cell and may result in a variation of its geometrical properties. Cell node addition and removal can be useful for several modelling needs, mainly to establish (or to maintain) a reasonable level of detail in cell representation. For instance, an intermediate node may be added to a cell c if one of its membrane edges is too long (i.e., if $|x_{c,i+1} - x_{c,i}|$ is larger than a threshold value for a given $i \in \{1, \dots, V_c\}$). In this case, the new membrane node may be located in a free grid vertex near to the middle point of the segment connecting i and $i+1$. On the opposite, node removal can be implemented in the case of too short cell membrane edges (i.e., if $|x_{c,i+1} - x_{c,i}|$ is smaller than a threshold value for a given $i \in \{1, \dots, V_c\}$). Further, changes in the number of cell membrane nodes can be dynamically suggested by the evolution of the simulated system. For instance, in the case of the migration of a polarized cell, it may be useful to create some nodes along the leading edge of the individual, i.e., to reproduce the extension of membrane motility structures such as filopodia, while removing nodes at its side and trailing surfaces. Finally, as it will be explained in the following, node addition may be required before cell division. Other rules and procedures for node creation and destruction can be eventually defined by researchers according to the specific phenomenon of interest.

Our approach also accounts for continuous elements, or *fields*, representing the spatio-temporal evolution of molecular entities, that may reside within discrete cell elements (as nucleic acids, cytosolic ions, and proteins), or in the external environment (as growth factors, matrix proteins, matrix metallo-proteinases). They are described as variable concentrations with standard *reaction-diffusion* (RD) equations, whose general form is

$$\frac{\partial g}{\partial t} = \underbrace{\nabla \cdot (D_g \nabla g)}_{diffusion} + \underbrace{F(c)}_{reaction\ term} , \tag{5}$$

where g denotes the local concentration of the molecular substance, D_g is its diffusion coefficient, and $F : \mathbb{R}_+ \to \mathbb{R}$ is the reaction term. Equations of type (5) may apply to the entire domain Ω or to selected subregions, with fixed or moving boundaries (as in the case of intracellular chemicals). As it will be explained in more detail later, these continuous equations can numerically solved using finite element schemes, which are properly employed on the selected domain discretization $\overline{\Omega}$.

2.1. The Metropolis algorithm

As in traditional CPMs, discrete cell-level objects rearrange and move to gradually reduce a system free energy which, as seen in the Introduction, can be described by a Hamiltonian functional H, that will be defined in detail below. The energy minimization procedure is here implemented by adopting a version of the Metropolis algorithm for Monte Carlo-Boltzmann thermodynamics properly modified to account for the selected cell representation. In fact, it evolves in time using repeated probabilistic updates of the spatial location of the cell membrane nodes. Procedurally, at each step t of the algorithm, called *Monte Carlo Step* (MCS), a membrane node i of a given cell c, which is actually located in a grid vertex j (i.e., $\mathbf{x}_{c,i}(t) = \mathbf{x}_j$), is randomly selected and proposed to *move* into an arbitrary *free* neighboring grid vertex location, say $\mathbf{x}_k \in \overline{\Omega}_j$. With the term "free" we here intend a grid vertex that is not occupied by a node belonging neither to cell c itself nor to another element $c' \neq c$. In particular, if the membrane node i is attempting to move to a free grid vertex located *within* the cell c itself, the element c is retracting, otherwise it is protruding, see Fig. 1 (D).

The move attempt is then accepted with a *Boltzmann transitional probability*, which has its origin in the statistical physics (see [42, 83] and references therein):

$$P(\mathbf{x}_{c,i} = \mathbf{x}_j \to \mathbf{x}_{c,i} = \mathbf{x}_k)(t) = p(T_c(t)) \min \left\{1, e^{-\Delta H(\mathbf{x}_{c,i}=\mathbf{x}_j \to \mathbf{x}_{c,i}=\mathbf{x}_k)(t)/T_c(t)}\right\}, \tag{6}$$

where ΔH is the net variation in the total energy of the system as a consequence of the cell membrane node move attempt and $T_c \in \mathbb{R}^+$ is a *fluctuation allowance*, which determines the extent of energy-increasing events leading to cell membrane displacement [70]. In this respect, it can be broadly correlated to the *intrinsic motility* of cell c (see [92] for a detailed comment). Further, as commented in [53], all the energy parameters relative to a cell c are scalable with the corresponding fluctuation allowance: therefore T_c can be fixed without loss of generality even if it does not have a direct experimental counterpart. Finally, $p(T_c(t)) : \mathbb{R}^+ \mapsto [0, 1]$ is a sort of *maximum transition probability*, a continuous and increasing function of T_c such that $p(0) = 0$ and $\lim_{T_c \to +\infty} p(T_c) = 1$. The specific form of (6) accounts for low motile individuals, i.e., which are not able to move even in the presence of favourable energy gradients [92].

For each node move attempt a further check has to be done in order to avoid the overlapping either of different parts of the membrane of the same cell or of parts of the membrane of different individuals. For instance, if cell membranes are represented by polygonal lines, as in our simplifying assumption, such a control can be done by simply checking if the segments linking the moving membrane node i to the consecutive ones (say, $i-1$ and $i+1$) intersect, as a consequence of the proposed configuration update, the edges forming the membrane of any cell of the system (including, the moving individual c itself). A membrane node move attempt that eventually results in membrane overlapping has to be rejected (even if it is in principle energetically favourable). Finally, as in traditional CPM approaches, a MCS may involve more than one cell node move attempt (for instance, Kawasaky dynamics are also possible [42]). The basic time step of the Metropolis algorithm needs then to be translated into actual units of time (i.e., seconds, hours, days) via proper a *posteriori* calibrations with experimental data.

2.2. The Hamiltonian

The algorithm described in the previous section determines the system evolution by iteratively and stochastically reducing an effective free energy. In this respect, the Metropolis method is independent from the specific form of the functional H (in principle, Eq. (6) holds also in the case of an energy not described by a Hamiltonian). However, since this work is focused on a modified version of the CPM, hereafter we will deal with energy functionals typically employed in the traditional framework. In particular, this section will be devoted to the description, and the adaptation to our computational environment, of some of the most common energetic contributions.

In the traditional CPM, a Hamiltonian H may contain a variable number of terms, which can be grouped in

$$H(t) = H_{\text{adhesion}}(t) + H_{\text{constraint}}(t) + H_{\text{force}}(t). \tag{7}$$

H_{adhesion} describes the adhesive/repulsive energy between couples of cell elements that interact across their membranes. H_{adhesion} is based on the Steinberg's *Differential Adhesion Hypothesis* (DAH) [43, 101, 102]. The DAH proposes that individuals in the same aggregate adhere to each other with different strengths, according to their specificity. The hierarchy of contact forces is one of the main driving mechanisms behind the evolution of biological systems, whose final organization is supposed to maximize the overall strength of interface interactions (or, in other words, to minimize the overall adhesion energy). Evidence supporting DAH has been observed in a wide array of biological systems: for example, it successfully explains how cellular adhesive properties can operate to determine tissue reorganization during cell sorting especially in the embryonic stage of life [4, 41, 42] (for a more detailed discussion on the DAH the reader can refer to the the last section of this work). The formulation of DAH-derived H_{adhesion}, proper for our node-based CPM, is

$$H_{\text{adhesion}}(t) = \sum_{(\mathbf{x}_j,\mathbf{x}_k) \in \overline{\Omega}^{c}(t) \times \left[\overline{\Omega}^{c'}(t) \cap \overline{\Omega}_j\right],\ c \neq c'} J_{(c,c')}(t), \tag{8}$$

where $\overline{\Omega}_j$ is, as seen, the first-nearer neighborhood of grid vertex j and therefore c and c' are two neighboring cell-scale elements (i.e., two cells or a cell and an extracellular element, say an insoluble matrix component). The coefficients $J_{(c,c')} \in \mathbb{R}_+$ are local binding energies and are symmetric with respect to their indices. As in traditional CPMs, they may depend on the cell types (i.e., $J_{(\tau(c),\tau(c'))}$) or be specific for the specific pair of interacting individuals. With (8), we are assuming that intercellular adhesive interactions are strictly localized at cell nodes, and not extended over the entire cell membranes (as instead happens in the classical version of the CPM). Such simplifying hypothesis is coherent with the proposed cell representation, being employed also in other vertex-based approaches for biological phenomena, see for example [28, 29, 37, 73] and the models reviewed in [36]. However, it is reasonable also from a biological point of view: in fact, cell adhesive molecules (CAMs), such as cadherins and integrins, diffuse from the cytosol to the plasma membrane and cluster in spatially-defined "hot spots" (i.e., focal adhesion points in the case of integrins and adherens junctions in the case of cadherins, see [32, 56] and references therein). In this respect, a possible model improvement is to define each family of CAMs as a continuous field, characterized indeed by a variable intracellular concentration. This way, it is possible to simulate the above-described diffusion of adhesion proteins from the cell internal regions to the plasma membrane. In this case, each parameter $J_{(\tau(c),\tau(c'))}$ can realistically vary in time and space, being a function of the local quantity of CAMs.

Remark. It is useful to recall that a pair of membrane nodes belonging to two neighbouring cells, say c and c', does not coincide but "only" shares the same grid element. As a consequence, although experiencing adhesive interactions, they maintain a distance equal to the characteristic size of the domain discretization. In this respect, the more the domain discretization is refined, the more a pair of adhering cells are close one to each other, thereby more realistically reproducing biological conditions.

The term $H_{\text{constraint}}$ sums the energetic contributions that describe selected attributes of cell-scale elements, such as their perimeter and area. As in the standard CPM, they are written as energetic penalties, which increase as a discrete individual deviates from its designed state, in a non-dimensional elastic form [92]:

$$H_{\text{constraint}}(t) = \sum_{z-\text{attribute}} \sum_{c} \lambda_c^z(t) \left[\frac{a_c^z(t) - A_c^z(t)}{a_c^z(t)} \right]^2, \tag{9}$$

where $a_c^z(t)$ is the actual value of the z-attribute of individual c and $A_c^z(t)$ is its target value, which may be fixed or time-variable. The parameters $\lambda_c^z \in \mathbb{R}_+$ are Lagrangian multipliers [61, 92]. They take the role of "generalized elastic moduli", which determine the weight of each energetic constraint, and thus the importance of the corresponding cell attribute. In particular, low values of a given λ_c^z allow the discrete unit c to deviate more from the configuration that satisfies the constraint z. On the opposite, high values of λ_c^z imply that the discrete element c has difficulties to deviate from the configuration that satisfies constraint z. Since each energetic contribution given in Eq. (9) smoothly decreases to a minimum when the relative attributes is satisfied, the modified Metropolis algorithm automatically drives any system configuration towards one that more closely satisfies the constraints included in the model. In this respect, the simulated systems are not usually able to exactly satisfy all the constraints of all the discrete elements at any given time step t, since different attributes may be in conflict: this leads to system configurations characterized by multiple energetic local minima. Asymptotically, each energy contribution in (9) approaches infinity when the actual value of the corresponding cell attribute vanishes: this is an advantage, as an infinite energy is required, for example, to shrink a cell to a point. However, each term in (9) approaches to one if the actual value of the relative cell attribute becomes very large. This bias would be eliminated with a normalization by the target value of the attribute, say by A_c^z. The choice of the specific normalization can be done according to the actual modeling needs. However, both options lead to non-dimensional energy contributions: therefore, all the λ_c^z's are coherently in units of energy. Finally, the form of Eq. (9) is the simplest quadratic potential one can think of. However, it can be easily replaced by more sophisticated potentials $U(a_c^z(t), A_c^z(t))$, with $U : \mathbb{R} \times \mathbb{R} \mapsto \mathbb{R}_+$, characterized by the property

$$U(A_c^z(t), A_c^z(t)) = 0. \tag{10}$$

Among others, the energetic contributions relative to selected geometrical attributes of discrete objects, such as their surface and perimeter, are of particular relevance:

$$H_{\text{surface}}(t) = \sum_c \lambda_c^{\text{surface}}(t) \left[\frac{s_c^{\text{surface}}(t) - S_c^{\text{surface}}(t)}{s_c^{\text{surface}}(t)} \right]^2 ; \tag{11a}$$

$$H_{\text{perimeter}}(t) = \sum_c \lambda_c^{\text{perimeter}}(t) \left[\frac{l_c^{\text{perimeter}}(t) - L_c^{\text{perimeter}}(t)}{l_c^{\text{perimeter}}(t)} \right]^2 . \tag{11b}$$

These terms depend on the actual measures of each cell-scale element, i.e., $s_c^{\text{surface}}(t)$ and $l_c^{\text{perimeter}}(t)$(that can be measured as previously described, cf. Eq. (4)), as well as on the corresponding target quantities, i.e., $S_c^{\text{surface}}(t)$ and $L_c^{\text{perimeter}}(t)$ (that can correspond to a relaxed/undeformed cell configuration or to an initial condition). In particular, the energy variation (11a) due to cell surface deviations from the target measure may be related to the work done by intracellular pressure [61]. $\lambda_c^{\text{surface}}$ indeed regulates the conservation of mass of the discrete element c and encodes all the bulk effects: in this respect, cell growth can be realistically included by assuming that $S_c^{\text{surface}}(t)$ increases during the simulation [23, 82]. The term (11b) can instead be interpreted as an elastic (Hookean) tension applied to the membrane of cell c, that accounts for its contractility. The cell remodeling ability is determined by the cortex acto-myosin complex, which can be in turn stimulated by internal (such as small G-protein activity) or external stimuli (such as ECM contact guidance), see [53, 57, 61]. From this point of view, $\lambda_c^{\text{perimeter}}$ represents a sort of inverse elasticity of c, i.e., of the ease with which it can change its shape. For instance, if $\lambda_c^{\text{perimeter}}$ is very large, c has a negligible elasticity, and its membrane is tight.

The Hamiltonian composed of Eqs. (8), (11a), and (11b) constitutes the basic framework of most CPMs. However, additional terms, here grouped in H_{force}, can be further introduced to model effective and generalized external forces that act on discrete elements. All these contributions can be described with the same architecture [30]:

$$H_{\text{force}}(t) = -\sum_{f-\text{force}} \sum_{c,\, \mathbf{x}_j \in \overline{\Omega}^c(t)} \mu_c^f(t)\, \mathbf{F}^f(t) \cdot \mathbf{x}_j, \tag{12}$$

where $\mathbf{x}_j$ is the application point of force $\mathbf{F}^f$ on cell c and $\mu_c^f \in \mathbb{R}$ measures the corresponding effective strength. For instance, an extracellular molecular substance (which is a continuous element described by a discretized PDE) can activate selected transmembrane receptors of a cell (which is a discrete object represented on the same grid), thereby biasing its movement: as a result, the cell chemotactically migrates upon chemical gradients. These dynamics can be implemented in our model by the following energetic contribution:

$$H_{\text{chemical}}(t) = -\sum_{c,\, \mathbf{x}_j \in \overline{\Omega}^c(t)} \mu_c^{\text{chem}}(t) g(\mathbf{x}_j, t), \tag{13}$$

where $g(\mathbf{x}_j, t)$ is the present concentration of the molecular substance (which evolves following a proper equation, cf. (5)) at cell membrane node location j and coefficient μ_c^{chem} is the effective cell chemical potential. In this respect, the net energy difference resulting from a chemotactic stimulus when a membrane node i of a cell c attempts to move is

$$\Delta H_{\text{chemical}}(\mathbf{x}_{c,i} = \mathbf{x}_j \to \mathbf{x}_{c,i} = \mathbf{x}_k)(t) = \mu_c^{\text{chem}}[g(\mathbf{x}_j, t) - g(\mathbf{x}_k, t)]. \tag{14}$$

Recalling the dissertations on the traditional CPM [42, 61, 92], the total force $\mathbf{F}_{c,i}$ applied at a membrane node i of a cell c is given by the negative local gradient of the energy function, calculated at the grid point actually occupied by i. For instance, considering a typical Hamiltonian, we have that

$$\mathbf{F}_{c,i}(t) = -\nabla H_{\mathbf{x}_j=\mathbf{x}_{c,i}}(t) \tag{15}$$

$$= -\nabla \left[\underbrace{H_{\text{surface}}(t)}_{\mathbf{F}^{\text{pressure}}} + \underbrace{H_{\text{perimeter}}(t) + H_{\text{adhesion}}(t)}_{\mathbf{F}^{\text{membrane}}} + \underbrace{H_{\text{force}}(t)}_{\mathbf{F}^{\text{ext. forces}}} \right]_{\mathbf{x}_j=\mathbf{x}_{c,i}} . \tag{16}$$

In particular, as stated from the above equation, the vector $\mathbf{F}$ can be decomposed into a pressure-driven term and in the contributions due either to extracellular forces or to the forces acting on the cell membrane (i.e., adhesion and cortical tension). It is however important to note that biological cells are highly dissipative objects, as they are characterized by a low Reynolds number [84]: indeed, viscosity greatly exceeds inertial forces and cell behavior is usually assumed to be overdamped, i.e., regulated by first-order dynamics [42, 61].

2.3. Further model ingredients

The proposed modeling framework can reproduce other biological processes, including cell duplication. In this respect, the main difficult relies in the choice of a specific algorithmic procedure that realistically implements the mechanisms of cell division. A possible option can be the following (see Fig. 2 (A), bottom panels): given a mitotic cell c, select a membrane node (say i) and link it to one of its non consecutive nodes (say, not to nodes $i+1$ or $i-1$), such that the new membrane edge does not overlap to the others. A close polygonal line is indeed obtained: it identifies one of the daughter cells. The other daughter individual is then given by the remaining part the parent's membrane, closed by a new segment that links the pair of consecutive disjointed nodes. Both cell and node renumbering are eventually required. As in the case of the traditional CPM, the daughter cells can evenly inherit all the parent's attributes and properties. As reproduced in the bottom panels of Fig. 2 (A), such a division mechanism may cause a substantial drop of cell mass: however, due to the shape constraints in Eqs. (11a)-(11b), the daughter cells gradually maturate into full-size individuals.

Further drawbacks of this procedure are that it can be implemented only in the case of cells defined by more than 5 vertices and that at least one of the two newly born individuals may be defined by a significantly low number of membrane nodes. In this respect, an algorithmic setup that gives to both daughter cells the same number of vertices (i.e., the half with respect to the parent's number) may be preferable. Node addition can be also useful to maintain a good detail in the representation of the daughter individuals. The procedure for cell duplication may take into account more sophisticated phenomenological rules as well. For instance, as suggested by a number of experimental works as early as [97], a stochastic distribution of the time between cell divisions, which may depend both on the genetic state of each cell and on the time from its last mitotic process, can be introduced. Further, a cell can be prohibited to proliferate in the absence of a sufficient quantity of growth factors, as widely demonstrated in literature with mitogenic assays (refer for example to [71, 100, 113]).

The proposed node-based model is able to employ also some other features characterizing the traditional CPM, as the compartmentalization approach introduced and described in [92, 93]. According to this method, a collection of standard discrete cell-level objects can be clustered to form a compartmentalized element, which can better reproduce a real biological individual. Technically, this approach requires that a set of discrete units c shares an additional attribute, a cluster id (say, $d \in \mathbb{N}$), which defines the compartmentalized individual they belong to, see Fig. 2 (B). As in the case of the standard version of the CPM, such a representation of individuals requires a redefinition of the characteristic terms of the Hamiltonian. First, it is necessary to differentiate the contributions of H_{adhesion} due either to the contact between the membranes of discrete units belonging to the same element, namely $H^{\text{internal}}_{\text{adhesion}}$, or to the contact between the membranes of discrete units belonging to different elements, namely $H^{\text{external}}_{\text{adhesion}}$. It is finally needed to specify the attributes and the forces characterizing all the subunits of each compartmentalized element. Such a technique allows to reproduce more realistic cell morphology and behavior. For instance, it is possible to study the role in cell migration of cytoskeletal elements, which provide support and mediate coordinated and directed movements in response to mechanical tensions and stresses from the local environment. A possible option is to employ two-compartmental cells, i.e., differentiated in the nucleus (say, element c) and in the cytosolic region (say, element c'), which are defined in our version of the CPM by the corresponding membranes, see Fig. 2 (B). In this respect, it is useful to remark that the nodes of the intracellular compartments can be located according to an experimental image, following the same algorithmic steps described in the text in the case of Fig. 1 (B). The following additional constraint in Eq. (9) has then to be included:

$$H_{\text{spring}}(t) = \sum_{(\mathbf{x}_j,\mathbf{x}_k)\,\in\,\overline{\Omega}^{c}(t)\,\times\,\overline{\Omega}^{c'}(t)\ ,\ c\neq c'} \lambda^{\text{spring}}_{c,c'}(t)\left[\frac{|\mathbf{x}_j-\mathbf{x}_k| - D^{\text{spring}}_{c,c'}}{|\mathbf{x}_j-\mathbf{x}_k|}\right]^2 . \tag{17}$$

It in fact plays the role of a spring connecting each node of the cell plasma membrane to each node of the nucleus membrane. In particular, $D^{\text{spring}}_{c,c'}$ represents the target (e.g., equilibrium) length of the connection, $\mathbf{x}_j$ and $\mathbf{x}_k$ are the location of the corresponding vertices, and $\lambda^{\text{spring}}_{c,c'} \in \mathbb{R}_+$ is a generalized elastic coefficient. The term (17) models the fact that the nucleus is anchored by intermediate actin filaments and microtubules to the cell plasma membrane, which is in turn linked to the extracellular substrate through the focal adhesion clusters, see the review [108] and the references therein. This way, it is possible to more realistically describe cell movement, i.e., to take into account simple cytoskeletal dynamics. Let us in fact suppose that an external stimulus causes the cell plasma membrane to locally protrude in a given direction: the overall cytosolic region indeed deforms and extends forward. However, due to the term (17), the nuclear membrane is pulled with the same force and therefore coordinately moves with the overall cell. However, a more realistic model should explicitly include acto-myosin dynamics and the relative signal transduction (this topic is often approached in the literature with multiphase models, see for example the book [2]). A possible option may amount to use the stress distributions at the plasma membrane as a signaling input for the subsequent cytoskeletal dynamics.

3. Sample simulations

In order to clarify the role in cell dynamics of the most relevant energetic contributions and parameters introduced in the previous section, we now illustrate some test simulations.

Hereafter, we employ rectangular domains Ω, with different sizes. For the sake of simplicity, all of them are discretized with a fixed triangular mesh, as the one presented in Fig. 1 (A), right panel, where each grid element has a characteristic size of 1 μm. Indeed, in all cases, the number of grid elements can be calculated as 2 × Area(Ω). In all the sets of simulations proposed in the following, the system evolves according to the Boltzmann-like transition probability (6), with one cell node move attempt for each MCS and $p(T_c) = \tanh(T_c)$ where, as already sketched, the motility parameter T_c is a measure of the agitation rate of individual c.

We first try to find out the possible equilibrium cell configuration (i.e., size and shape) at selected parameter regimes. We indeed study the behavior of a single cell $c = 1$ placed within a 100 μm × 100 μm-domain, see Figure 3. The cell is defined by $V_{c=1} = 14$ membrane nodes, whereas the Hamiltonian accounts for the geometrical constraints specified in Eqs. (11a)-(11b). In particular, the initial measures of the cell correspond to half of its (fixed) target dimensions: $l_{c=1}^{\text{perimeter}}(t = 0) = L_{c=1}^{\text{perimeter}}/2 = 90$ μm and $s_{c=1}^{\text{surface}}(t = 0) = S_{c=1}^{\text{surface}}/2 = 700$ μm^2. Both the cell fluctuation allowance and the elastic moduli λ's are constant in time. As reproduced in Fig. 3, when $T_{c=1} \approx 0$, the cell is almost freezed, regardless of the value of the other parameters. To observe significant cell dynamics, it is therefore needed to have a sufficiently high value of the cell fluctuation allowance. In this respect, given the lack of a direct experimental correspondence [107], its estimate might represent an issue. However, as provided in the case of the traditional CPM [53, 107], all energy contributions relative to a cell c can be scalable with T_c, whose value can therefore be fixed without loss in generality. In this respect, the fluctuation allowance of each model cell will be hereafter set equal to 25. The other model parameters will instead vary, according to the specific simulation: however, they will fall within a reasonable region of the space of possible values. For a given cell c, it would be in fact nonsensical to have $T_c \in [0, 100]$ and, e.g., the λ-coefficients characterized by a difference of three or four orders of magnitude. This appropriate precaution is employed also in most published CPM works (see for instance [61, 68, 69, 106]), as it also avoids undesired numerical effects, such as cell death and disappearance in the long run [107]. The behavior of a cell is then mainly determined by the hierarchy (and not by the specific values) of the model parameters relative to its energy contributions. In other words, cell dynamics do not vary if all the relative model coefficients are scaled by the same factor. In this respect, if $T_{c=1}$ is high (say, $= 25$), a critical role is played by $\lambda_{c=1}^{\text{surface}}$: if it is comparable to the fluctuation allowance (say, $= T_{c=1}$), the cell rapidly reaches its target measures. After this transient, the cell morphology then stabilizes if also $\lambda_{c=1}^{\text{perimeter}}$ falls within the same range (say, $= T_{c=1}$), while it undergoes random perimeter fluctuations that, however, preserve its area, if

$\lambda_{c=1}^{\text{perimeter}} \ll T_{c=1}$, see the corresponding panels in Figure 3. On the opposite, if $\lambda_{c=1}^{\text{surface}} \ll T_{c=1}$, the cell undergoes sudden and unrealistical mass variations, regardless of the value of $\lambda_{c=1}^{\text{perimeter}}$ (not shown).

As stated above, the hierarchy of the values of the binding energies J's in the DAH-derived term (8) describe the relative preference of cell-level objects for creating adhesive boundaries with other discrete individuals. To analyze how specific variations of such contact strengths affect the dynamics, as well as the final configuration, of a biological system, we first examine the evolution of a round aggregate of 50 cells, all of the same type $\tau(c) = L$ ("L" for light), placed in the center of a 2.025×10^5 μm^2 domain, see Fig. 4. Each individual is identified by $V_c = 5$ membrane nodes. The Hamiltonian of the system accounts both for cell geometrical attributes and for intercellular adhesive interactions. As usual, the rule in Eq. (6) holds, with $T_c = T_L = 25$ for all $c = 1, \ldots, 50$. In particular, for the sake of simplicity, the initial and the target cell measures coincide: they are equal to $l_c^{\text{perimeter}}(t = 0) = L_c^{\text{perimeter}} = L_L^{\text{perimeter}} = 60$ μm and $s_c^{\text{surface}}(t = 0) = S_c^{\text{surface}} = S_L^{\text{surface}} = 300$ μm^2 for all $c = 1, \ldots, 50$. Taking advantage of the results summarized in Fig. 3, we then set for all cells c a high $\lambda_c^{\text{surface}} = \lambda_L^{\text{surface}} = T_L = 25$ to preserve their area and a low $\lambda_c^{\text{perimeter}} = \lambda_L^{\text{perimeter}} = 0.5 \ll T_L$ to allow significant remodeling and membrane fluctuations. We further assume that the intercellular contact strength is the same for all pairs of interacting individuals, depending on their type. In particular, referring to Eq. (8), we have that $J_{c,c'} = J_{(\tau(c),\tau(c'))} = J_{L,L}$ for any pair of neighboring cells (c, c'). As reproduced in Fig. 4 (top panels), if $J_{L,L} \ll T_L$, which means a high intercellular adhesion, and hence an overexpression of cadherin molecules, the aggregate remains compact and strictly packed. In particular, the component cells deform trying to maximize intercellular connections, as they have energetic benefits to stay attached one to each other. On the opposite, for larger values of cell-cell adhesion (i.e., $J_{L,L} = T_L$, which represent the model counterpart of a downregulation in the cadherin activity), the aggregate quickly dissociates into isolated individuals, displaying a scattered phenotype. In fact, not only external cells spread away, but a repulsion occurs also among individuals within the core of the population. The cells in fact energetically prefer to float within the extracellular environment rather than creating intercellular bonds. The dispersion of single cells upon low intercellular adhesion is of particular relevance, for instance, in the early stages of solid cancer growth and development. As described in detail in the experimental literature (refer to [20, 21, 26]), the malignant individuals able to escape from the main tumor mass have in fact the greatest invasive potential, as they can invade the host tissue and further metastasize.

To further compare our method to the standard version of the CPM, we next perform simulations of cell sorting (the literature on the topic is vast, the interested reader can refer for instance to [40, 43, 57] and references therein). In this respect, a cellular aggregate formed by two types of randomly positioned individuals, namely $\tau = L$ (light) and $\tau = D$ (dark), is placed within a square domain whose size is equal to 450 μm. The Hamiltonian again regulates the geometrical attributes of cells and their adhesive behavior. We also set $T_c = T_L = T_D = 25$ for any c. The cell geometrical constraints and target measures (which correspond to the initial dimensions) are in common for all individuals, regardless of their type. They are the same as in the set of simulations shown in Fig. 3: in particular, we use high values of $\lambda_c^{\text{surface}} = \lambda_L^{\text{surface}} = \lambda_D^{\text{surface}} = T_L = T_D = 25$ and low values for $\lambda_c^{\text{perimeter}} = \lambda_L^{\text{perimeter}} = \lambda_D^{\text{perimeter}} = 0.5 \ll T_L = T_D$, for all $c = 1, \ldots, 50$. Finally, we capture the final system configuration at 5000 MCS. If the adhesive strength between the two cell types is higher than the two self-contact values (i.e., $J_{L,D} \ll J_{L,L} = J_{D,D} = T_L = T_D$), the cells heterogeneously mix to form an experimentally observed "checkerboard" (see Figure 4, bottom panel). This is due to the fact that making heterotypic bonds is more convenient from an energetic point of view than making homotypic bonds. On the opposite, if the homotypic adhesion is stronger than the heterotypic one (i.e., $J_{L,L} = J_{D,D} \ll J_{L,D} = T_L = T_D$), we observe a spontaneous cell sorting, with the formation of small clusters of cells of the same type, see the corresponding panel in Figure 4. Other cell aggregate configurations may be obtained by defining the extracellular medium as a discrete element, thereby introducing its adhesive relationship with the cells. As explained in more details in the conclusive section of this work, alternative mechanisms regulating cell organization can be in principle implemented in our computational framework: however, the proposed simulations have been based on the DAH to provide a closer comparison with the outcomes obtained with traditional CPMs.

As a further test simulation, we model the differentiated dynamics of a set of three cells upon an exogenous chemical stimulation. The three cells are initially aligned in a 1.2×10^4 μm^2 domain Ω, as shown in the first panel of Fig. 5. In particular:

- the left one, $c = 1$, of type $\tau(c = 1) =$ E (say, epithelial) is defined by

$V_{c=1} = 15$ nodes and is the only one sensitive to the chemical substance;

- the central one, $c = 2$, of type $\tau(c = 2) = \mathrm{F}$ (say, endothelial), is defined by $V_{c=2} = 12$ nodes;
- the right one, $c = 3$, of type $\tau(c = 3) = \mathrm{E} = \tau(c = 1)$, is defined by $V_{c=3} = 9$ nodes but is insensitive to the chemical.

In this case, the Hamiltonian is given by the sum of the terms describing intercellular adhesive contacts, cell morphological transitions and chemotactic response. As usual, the contact strengths depend on the type of interacting cells. In this respect, we set $J_{E,E} \ll J_{E,F}$, since we here assume that individuals of the same cell lineage express analogous cadherin molecules and therefore adhere more strongly. Further, according to the results obtained in the previous sets of simulations, we opt for the following parameter setting:

$l_{c=1}^{\text{perimeter}}(t = 0) = L_{c=1}^{\text{perimeter}} = l_{c=2}^{\text{perimeter}}(t = 0) = L_{c=2}^{\text{perimeter}} = 100\ \mu\text{m}$;
$l_{c=3}^{\text{perimeter}}(t = 0) = L_{c=3}^{\text{perimeter}} = 80\ \mu\text{m}$;
$s_{c=1}^{\text{surface}}(t = 0) = S_{c=1}^{\text{surface}} = s_{c=2}^{\text{surface}}(t = 0) = S_{c=2}^{\text{surface}} = 500\ \mu\text{m}^2$;
$s_{c=3}^{\text{surface}}(t = 0) = S_{c=3}^{\text{surface}} = 500\ \mu\text{m}^2$;
$\lambda_{c=1}^{\text{perimeter}} = \lambda_{c=3}^{\text{perimeter}} = \lambda_{E}^{\text{perimeter}} = 0.5 < \lambda_{c=2}^{\text{perimeter}} = \lambda_{F}^{\text{perimeter}} = 25$;
$\lambda_{c=1}^{\text{surface}} = \lambda_{c=3}^{\text{surface}} = \lambda_{E}^{\text{surface}} = \lambda_{c=2}^{\text{surface}} = \lambda_{F}^{\text{surface}} = 25$;
$T_{c=1} = T_{c=3} = T_E = T_{c=2} = T_F = 25$.

With the above hierarchies of coefficients, we are hypothesizing that, in the absence of nutrients, cell surface fluctuations are negligible and that the epithelial-like individuals are more elastic (i.e., they can more easily deform) than the endothelial one. Referring to Eq. (13) and recalling the previous assumption, we then have that $\mu_c^{\text{chem}} \neq 0$ (i.e., $= 4$) only for $c = 1$. The molecular substance finally evolves according to the following reaction-diffusion equation (RD):

$$\frac{\partial g}{\partial t} = D_g \nabla^2 g - \varepsilon_g g + p(g), \tag{18}$$

where the coefficients of diffusivity, $D_g = 10\ \mu\text{m}^2\ \text{s}^{-1}$ and of degradation $\varepsilon_g = 1.8 \times 10^{-4}\ \text{s}^{-1}$ are homogeneous throughout the domain. Their values have been estimated according to *in vitro* measures performed in [95] in the case of vascular endothelial growth factor isoforms (VEGFs). p describes instead the production of the chemical at a constant rate $\phi_C = 0.78$ h^{-1} (such a value has been experimentally quoted in [95] and widely used also in the modeling literature [38, 90, 91]) by a source extended along the entire right border of the domain. As already mentioned and discussed in more details in the next section, Eq. (18) is solved with a finite element scheme on the same domain discretization $\overline{\Omega}$ used for the node-based CPM. 10 diffusion step are run for each MCS, which is then set to correspond to 10 seconds, so that the resulting cell velocity falls in the realistic range 15 - 20 μm/h [81]. As shown in Fig. 5, the chemical-sensitive epithelial cell ($c = 1$) undergoes a gradual transition from the initial almost round stationary state to a polarized morphology, characterized by clearly distinguishable leading and trailing edges. In particular, the cell membrane protrudes at the front, defining the direction of migration towards the chemotactic source. The moving individual then avoids contacts with the endothelial cell, due to their low adhesive affinity, see Fig. 5 (top-right panel). On the opposite, attraction and subsequent adhesion occur between the two epithelial cells. In particular, cell $c = 3$, which is insensitive to the chemical stimulus, attaches to cell $c = 1$ and reorganizes in an elongated shape to maximize the adhesive contact between its nodes and those of individual 1. Finally, as captured in the last panels of Fig. 5, the individual $c = 3$ is dragged by cell $c = 1$ towards the source of the chemical (i.e., towards the right border of the domain).

4. Computational implementation and performance analysis

Originally, CPM users wrote their own software programs, which were specifically built according to the specific application they were developing. However, as commented in [5], these proprietary versions were usually incompatible, making the exact replication of published results hard and the integration of new CPM extensions considerably difficult. In order to obtain a common program, several groups have then released open-source, extensible CPM-based packages. Among others, the CompuCell3D[3] environment (CC3D) has recently become a standard simulation environment for the implementation of basic CPM applications. CC3D was jointly set up by groups at the University of Notre Dame[4] and at the Biocomplexity Institute at Indiana University at Bloomington[5], and it is still under full and active development.

---

[3] http://www.compucell3d.org

[4] http://www.nd.edu

However, the node-based version of the CPM presented in this work required an own implementation, as modifications of the already existing CPM-based softwares were not sufficient. Without entering in details, the core modules of the method (i.e., the set up of the domain and of the relative mesh, the implementation of the Metropolis algorithm and the definition of the specific Hamiltonian used in each simulation) are implemented in a C++ language. An XML-based markup language and reasonably simple Python scripts are instead used to introduce and control the model parameters. In particular, the implementation of our method consists of the following main algorithmic steps:

1. The discrete CPM evolves through a MCS, following the rule in Eq. (6), with the relative cell membrane edge intersection check;
2. Cell node addition, removal and renumbering is performed (if needed);
3. The biophysical properties of each discrete individual (e.g., surface, perimeter, polarization, velocity) are recalculated;
4. The equations of the continuous elements included in the simulation environment are rederived, according both to the relative kinetics laws and to the new boundaries of the cell-level discrete objects. They are then solved using a finite element method (FEM, [31]), employed on the domain mesh used for the node-based CPM and characterized by a number of diffusion time steps sufficient to guarantee numerical stability;
5. The Hamiltonian functional is updated, given the new configuration of the domain, and the system is ready to evolve again.

To study the numerical efficiency of the proposed algorithm, we analyze the performances obtained either from our method or from the traditional CPM in comparable simulation settings. In this respect, the following three cases are compared:

- The cell sorting simulation as presented in Fig. 4 (bottom-right panel);

---

[5] http://www.biocomplexity.indiana.edu

- A simulation consisting of a slight modification of the previous case, i.e., in which at each MCS a cell is randomly chosen and its membrane nodes are entirely renumbered;
- A cell sorting simulation implemented with the traditional version of the CPM and run from CC3D. In particular, in order to have a coherent system configuration, we employ a domain of 450 × 450 lattice sites, where each grid pixel has a characteristic size of 1 μm. The initial aggregate condition consists of an almost round colony formed by 25 light (i.e., $\tau = L$) and 25 dark (i.e., $\tau = D$) cells, with an initial surface of 300 pixels (i.e., corresponding to 300 μm^2). Finally, the Hamiltonian of the system is composed of the terms regulating intercellular adhesion and shape remodeling:

$$\begin{aligned} &H_{\text{trad CPM}}(t) = H_{\text{adhesion}}(t) + H_{\text{shape}}(t) \\ &= \sum_{\mathbf{x}\in\sigma,\mathbf{x}'\in\sigma'} J_{\tau(\sigma(\mathbf{x})),\tau(\sigma'(\mathbf{x}'))}(t) \\ &+ \sum_{\sigma} \left[\lambda_{\sigma}^{\text{surf}}(t) \left(\frac{s_{\sigma}^{\text{surf}}(t) - S_{\tau(\sigma)}^{\text{surf}}}{s_{\sigma}^{\text{surf}}(t)} \right)^2 + \lambda_{\sigma}^{\text{per}}(t) \left(\frac{l_{\sigma}^{\text{per}}(t) - L_{\tau(\sigma)}^{\text{per}}}{l_{\sigma}^{\text{per}}(t)} \right)^2 \right], \end{aligned} \tag{19}$$

  where, recalling the notation of the traditional CPM, $\mathbf{x}$ and $\mathbf{x}'$ are two neighboring lattice sites and σ and σ' two neighboring cells. The parameters (19) are taken exactly the same as the corresponding ones in the case of the simulation shown Fig. 4. In particular, we opt for $J_{L,D} = 25 > J_{L,L} = J_{D,D} = 0.5$, while we neglect cell-medium adhesiveness.

For each implementation setting, 50 realizations are run and stopped after 5000 MCS, an observation time sufficient to have a complete cell sorting. Then the average of the execution time obtained in the different cases is calculated and reported in Fig. 6 (the standard deviations are smaller than 5% and therefore not indicated). The experiments are carried out in a dedicated laptop (SSD 4GB RAM, Pro Intel i7). By comparing the resulting performances shown in Fig. 6, it is possible to note that our version of the CPM algorithm is ≈ 12% slower than the traditional CPM. Such a difference is further increased in the case of node renumbering. The underlying reasons are the following. In our method, the basic step of the Metropolis algorithm (i.e., a cell membrane node displacement attempt) is characterized by a complexity of $O(N^{d-1})$ (where d is the spatial dimension), as only cell boundaries are set to move (see the comment in [22]). However, the main computational burden consists in the fact that the required membrane edge intersection test and the cell node renumbering procedure introduce further steps characterized by a complexity of $O(N^d)$ (i.e., $O(N^2)$ in the case of two-dimensional simulations). The efficiency of the entire method is therefore drastically reduced (unless more appropriate data structures will be used).

To conclude the performance analysis of our version of the CPM, the graphs in Fig. 6 compare the execution time obtained by employing the sorting simulation of Fig. 4 (i.e., without cell node renumbering) upon variations in the number of cells, the number of nodes used to define each cell and the number of grid elements. Also in this cases, 50 realizations are performed and run for 5000 MCS, while the corresponding execution times are calculated and then averaged. On one side, increments in the domain elements do not affect the algorithm efficiency. This is due to the fact that, unless in the case of time-evolving or adaptative meshes, the system has not to recalculate the position of the grid vertices. On the opposite, as expected, increments in the number of cells or in the number of their membrane nodes result in a slowdown of the algorithmic performance. To mitigate this issue, a preliminary study of the problem of interest may be very useful. For instance, if a given biological phenomenon requires an accurate description of the subcellular scale, it should also allows to take into account a small number of individuals. On the opposite, if the simulation of a huge population is needed, the level of detail for each component cell can be significantly decreased. However, we are aware that it is not always possible to maintain the complexity of the simulated system within a reasonable range. Efficient computational techniques that are able to significantly increase the simulation speed would be therefore needed.

One of the main issues of the algorithm underlying our version of the CPM is that too low acceptance probabilities of cell membrane node displacement often waste much computational time. As commented in [5, 24], this problem holds also for the traditional CPM and has been addressed by several approaches that may be implemented in our method as well. In this regard, *rejection free* dynamics, such as *N-fold way* and *kinetic Monte Carlo*, are particularly productive [7, 35, 59]. For each time step, they in fact do not consider a trial index copy, which may or may not be accepted, but choose only from the set of allowed lattice updates (i.e., those that decrease the system energy). The net computational gain will indeed depend on the balance between the average number of possible cell number flips and the average acceptation rate. The *Masking* algorithm instead focuses in reducing the inefficiency of the Metropolis algorithm by avoiding computation of energy between lattice sites within the same discrete object [112]. However, this technique still requires a large number of attempted exchanges. The *Random-Walker* (RW) algorithm instead reduces, but does not eliminate, the rejection rate by selecting as target sites only those belonging to an object boundary [22, 45]. The automatic rejection of non-boundary sites, characteristic of the standard CPM algorithm, is therefore eliminated.

The increment of the computational speed is however appreciable only in the presence of significantly large domains, containing a huge number of simulated individuals as well. For this reason, most of the above-commented methods are integrated by the use of distributive computing, where the overall simulation domain is typically divided and distributed between the nodes of a cluster of CPUs [5, 45, 55]. The already-cited Masking algorithm [112] represents for instance the first parallel version of the original Potts approach. It is used to simulate a model of grain growth, where the effective energy consists only of local interactions between grain boundaries. In this respect, as explained in [5, 24], the main difficulty of all forms of CPM parallelization is that the effective energy is nonlocal: when a given object crosses between CPU nodes, any modification to it in fact requires efficient parameter passing, so that the overall computation does not use stale values. Therefore, a naive parallelization, where the activity of each processor is restricted to a predefined subdomain of the whole lattice, increases the frequency of interprocessor communication for synchronization: the waiting time of each CPU will be therefore much greater than its calculating time. An interesting attempt to overcome this issue is made with the *checkerboard algorithm*, presented in [24]. Its developers use an improved data structure to describe simulated individuals as well as a further decomposition of the subdomain assigned to each CPU. In particular, the resulting sublattices are chosen so that the corresponding ones on different processors do not interact. In this way, an update in one sublattice affects only a selected (i.e., *a priori* established) set of sublattices. Each CPU node is therefore able to determine the cell identification number flips affecting neighboring nodes, accumulate them, and pass them synchronously. In this case, the speed gain increases with the size of the subgrids per processor and decreases with the interaction range. The checkerboard parallelization can also implement rejection-free or

RW methods, by using either equivalent or master-slave computations. In [24], the authors claim that the checkerboard execution scheme minimizes communication due to synchronization between the CPU nodes and show that, due to the stochastic nature of the simulation, model accuracy does not suffer much if synchronization does not takes place at every time step. Their analysis is based on the assumption that lattice sites updates are rare occurrences at the boundaries between regions. However, as commented in [22], this assumption may not hold true for large-scale simulations. A recent RW distributing implementation of the CPM runs significantly faster [45]. However, the proposed parallel scheme requires shared memory with all processors sharing the same subdomains: it is indeed needed a copy of the entire lattice in each CPU, which limits scalability.

The use of parallel computing can of course help to improve the efficiency of the algorithm underlying our node-based CPM. However, according to us, distributed computing has to follow a preliminary computational optimization of our method, at least in the steps concerning the cell membrane overlapping test and the eventual cell node renumbering.

5. Discussion

The macroscopic evolution of multicellular tissues and organisms is determined by processes characteristic of different spatiotemporal scales. In this respect, a wide range of of mathematical models waive the fine detail of microscopic mechanisms while focusing on cell-level dynamics, i.e., on the cell biophysical properties and behavior. These mesoscopic theoretical approaches are powerful instruments for comprehending and reproducing biological phenomena: they in fact facilitate the comparison between model outcomes and experimental data, given the immediate interpretation of the simulation results and the reduced number of variable and effective parameters, as commented in [61]. One of the principal families of mesoscopic mathematical methods is constituted by Individual Cell-Based Models (IBMs, also called Cellular Automata with an abuse of terminology), whose main feature is the possibility to preserve the identity of the individual cells forming the system of interest [1, 33]. The IBMs can be classified in different categories: those in which each cell is correlated to a single spatial unit (e.g., a material point or a center of mass-based entity) and those in which each cell is instead defined by a collection of spatial units. This last group of approaches includes the cellular Potts model (CPM). It in fact represents cell-level objects as sets of contiguous lattice sites that share the same identification number. Each discrete element is therefore allowed to have a degree of freedom to deform, which is only limited by the spatial resolution of the domain. In this respect, the CPM can be indeed considered a member of the Cell Surface Mechanics (CSM) models which, as commented by Lecuit and Lenne in [58], describe how biologically-generated tensions (resulting from intercellular adhesion and intracellular pressure and cortical contractility) affect cell shape and dynamics.

In this foundational work, we have proposed a substantially modified version of the CPM, which relies on a node-based representation of cell-scale elements. In this respect, the CPM simulation domains no longer need to be fixed and regular (square or hexagonal) numerical lattices but can be any physical region, provided with a proper discretization. Possible domain meshes of our CPM-based method may include irregular or deformable grids and graphs of all classes, even adaptive according to the dynamics of interest. The proposed cell representation results in some further consequences. First, realistic cell morphologies can be obtained by grid refinements and by setting a large number of membrane nodes for each individual, always keeping in mind that the more the simulated system is detailed the more the simulations are computationally expensive (cf. Section 4). Secondly, the vertices of the discretized domain can be empty, i.e., not occupied by any cell node. It is indeed not necessary to introduced a medium element, i.e., the classical generalized cell $\sigma = 0$ of the standard CPM, which often forces CPM authors to set an unrealistically high cell-medium energy cost to prevent the presence of extracellular sites within cell aggregates, as done for instance in [6]. In this respect, the extracellular environment can be defined and characterized only when it is really needed, for instance, when haptotactic or durotactic phenomena are of interest or when it is composed of insoluble matrix proteins (e.g., laminin, fibronectin, collagens). Entering in more details, single ECM fibers may be easily represented by segments connecting two o more grid vertices (according to the scale of the domain).

Another difference of the node-based CPM with respect to the standard version of the method is that, when moving, cell-scale elements do not superimpose one another. In fact, a cell membrane node can only move in the free space (when extending) or within the body of its own individual (when retracting) but it can not occupy a location belonging to another discrete element. In this respect, each discrete cell is characterized by its own membrane, that realistically rearranges (via node location updates) and eventually pushes onto the neighboring individuals, to produce collective cell movement.

A further advantage of our approach with respect to the traditional CPM which, as seen, is based on rigid lattices formed by fixed and equivalent (square or hexagonal) sites, is the possibility of interfacing it with purely continuous approaches, not limited to RD equations reproducing the evolution of chemical variables (that are already included in most CPMs). Our node-based CPM can be in fact employed on the domain discretization that best fits the numerical needs of proper fluid dynamics models (e.g., Navier-Stokes, Darcy, or Brinkman equations) and/or of selected continuum mechanics methods that can describe, for instance, the extracellular matrix (and its elastic, elastoplastic, or viscoplastic properties).

Regardless of the different representation of cell-scale elements, our CPM-derived method is still based on the classical Metropolis algorithm, which results in overdamped cell dynamics and in an implicit dissipation (as commented in [52, 61, 93]). As in the case of the traditional version of the CPM, it is indeed difficult to represent and control viscosity also in our approach. In this respect, possible options may include the introduction of an energy threshold in the exponential term of Eq. (6) or the addition of a proper contribution in the Hamiltonian. The Metropolis algorithm can of course be used to implement several energy functionals. However, in this work, we have only employed Hamiltonians formed by terms typically used by CPM authors, i.e., that deal with cell geometrical constraints, chemotactic stimuli, and intercellular adhesiveness. In this respect, the Differential Adhesion Hypothesis is one of the fundamental assumptions of most CPM applications. It proposes that cell sorting results from the hierarchy of adhesive strengths between the different cell types. However, the DAH is only one of the possible mechanisms underlying tissue organization and its acceptance is controversial [11]. For instance, Harris proposes a Differential Surface Contraction (DSC) hypothesis, in which cortical tension (the force generated within cells whose direction is parallel to their surface), rather than differential adhesion, drives multicellular patterning [46]. From this point of view, cell sorting is similar to active migration, which is significantly driven cell morphological transitions. The DAH instead holds also if cells are considered as structureless units. In this respect, an interesting paper by Krieg and coworkers [57] tests both the DAH and the DCS assumption by experimentally measuring (with an atomic force microscope) the adhesiveness and the cortical tension of cells from three germ layers of zebrafish embryos and then by performing pairwise sorting assays. From their coupled *in vitro – in silico* results, it seems that cell organization is mainly driven by the DCS (or by similar assumptions, such as the Differential Interfacial Tension Hypothesis [12]) rather than by the DAH. However, as lucidly commented by Green [44], the experiments by Krieg and colleagues fail to reproduce *in vivo* dynamics, probably because they barely take into account of time-dependent variations of intercellular adhesiveness, of other factors determining cell deformability and of the fact that the adhesion of cell sheets is quite different from that of individual cells. Summing up, it still remains debated whether differential adhesion and cortical tension are mutually exclusive or act in synergy (may be in conjunction with other mechanisms) to determine cell sorting and organization.

Focusing on CPMs, it has to be said that the DAH still remains one of the fundamental assumptions: only recently, cortical tension has begun to be included in the modeling framework, as done by Krieg and coworkers in the already cited paper [57]. Original CPM simulations in fact successfully captured cell sorting phenomena by taking into account only of intracellular pressure and intercellular adhesiveness [40, 43]. Ouchi and coworkers then first proposed an extension of these approaches, that amounted in the addition of an energy contribution representing a perimeter constraint [79]. Such a term was identified to model cortical tension, and since then has been extensively used in several multicellular computational studies. For instance, in [53] Käfer and coworkers use a 2D CPM to study the critical parameters determining Drosophila eye geometry, which is essential for correct vision. In particular, the basic unit of the Drosophila retina, the ommatidium, is formed by 4 cells surrounded by 2 primary pigment cells, embedded in a hexagonal matrix consisting of secondary and tertiary pigment cells [109]. This pattern is close to a 2D foam layer: therefore, the authors make the hypothesis that surface tensions, which drive soap bubble packing [25, 58], are responsible also of cell sorting and organization in Drosophila morphogenesis. In particular, Käfer and colleagues first assume that cell surface tension is modified only by adhesion, i.e., they use a Hamiltonian only accounting for cell-cell contact interactions and area constraints. As a result, the cells mechanically behave as soap bubbles: they meet by three at each vertex at almost equal angles. However, such model outcomes fail to reproduce the experimentally observed patterns resulting from different cadherin expressions. The reason is that cells greatly differ from bubbles, both in their membrane and in their internal composition. In this respect, Käfer and coworkers argue that, as commented also by Lecuit and Lenne in [58], cell surface tensions results from the opposite action of adhesion and cytoskeletal dynamics, i.e., from an adhesion-driven extension of cell-cell interfaces balanced by a cortical contraction. The authors indeed add an elastic potential regulating cell perimeter length. The resulting model finally explains correctly the geometry both of wild type and of mutant ommatidia. The minimization of a Hamiltonian energy that include a balance between intercellular adhesion and intracellular pressure and cortex contractility is at the basis also of a CPM analyzing Drosophila wing, set up by Bardet and coworkers [6]. In particular, these authors show that the loss of the tumor suppressor PTEN disrupts regular cell rearrangements by inhibiting a localized decrease of Myosin II and Rho-kinase, and therefore by preventing the lengthening of newly formed cell-cell junctions. A homogeneous distribution of MyoII is in fact required for a homogeneous cortical contractility and therefore for the formation of a stable, honeycomb-like cell packing, as observed in several epithelial tissues [27, 39, 72].

Further comments are needed on the specific Hamiltonian terms proposed in this work, especially on the relative parameters. First, both the intercellular adhesive strengths and the generalized spring moduli λ's have been assumed non negative: this choice has been done to maintain a closer comparison with the parameter settings usually employed in traditional CPMs. However, it is useful to recall that there has been ample discussion whether it is more reasonable to use positive or negative J-values [53, 79, 86], because it is difficult to experimentally quantify them, see also [62] for a detailed comment. In this respect, the already-cited scholar study by Magno and coworkers show both analytically and through simulations that concurrently changes in all J-coefficients (and therefore also a shift from positive to negative values) do not affect the dynamics of the system, if such parameter variations are accompanied by a proper rescaling of cell volume and surface (i.e., area and perimeter in 2D). A similar analysis in the case of our node-based CPM would be interesting as well, although we expect to obtain analogous results. In the case of compartmentalized approach, it is however consistent to use negative values for the intracellular contact strengths (i.e., in the case of the contact between subunits belonging to the same individual) and positive values for intercellular adhesiveness, see [92, 93]. In the same work, Magno and colleagues claim that it is nonsensical to consider negative values for perimeter and area constraints [61], thereby confirming the coherency of our assumptions. Finally, the sing of the Lagrangian multipliers in Eq. (12), which give the cell response to a given external force, has to be determined according to the dynamics of interest. For example, in the case of a chemotactic stimulus, $\mu_c^{\mathrm{chem}} > 0$ yields cell c to move up the gradient of the molecular substance (which is therefore a chemoattractant), whereas $\mu_c^{\mathrm{chem}} < 0$ results in its movement in the opposite direction (and the molecular substance is chemorepellent).

Regardless the above considerations, both in the case of the traditional CPM and in the case of our node-based version, a direct one-to-one correspondence between some model parameters and experimental quantities is not straightforward (as commented also in [41, 42, 67]). In particular, as explained in details in [107], the CPM parameters can be subdivided in (i) directly interpretable and measurable quantities, such as cell geometrical dimensions or kinetics coefficient of continuous fields, and (ii) more technical parameters that only subsume various cellular and subcellular properties, such as the adhesive strengths and the Lagrangian multipliers relative to cell attributes and cell response to selected forces. It is indeed consistent to assign to the first group of parameters actual dimensioned units, whereas the second group scales in dimensionless units of energy. This choice, largely employed also in traditional CPM works (see, as a representative example the scholar work by Magno and colleagues [61]), has been made to allow researchers to reasonably fix at least the set of parameters with a possible and direct experimental counterpart: as a consequence, the degrees of freedom of the parameter space, as well as the complexity of the relative sensitivity analysis, are reduced. In this respect, as commented in [107], the CPM coefficients included in the energy terms interfere each other in an intricate way, and therefore simultaneous parameter fittings are often needed to disclose knowledge on the model behavior. However, at present, there is not a proper algorithm for an optimal parameter estimate for CPM approaches, which indeed still remains a complex task, actually requiring "much intuition and skills by the authors themselves" [107]. In this perspective, we have here proposed simulations to elucidate how specific parameter settings translate into qualitative system dynamics. First, we have shown that too low values of the fluctuation allowance, that weights the probability of accepting a trial displacement causing an energy gain, result in cell freezing. However, in this case, we have not captured undesired grid effects, as observed instead with the traditional CPM [61, 64]. Further, the simulations presented in Fig. 3 have linked the evolution and the stabilization of cell morphology to selected ranges of values both of the cell elastic moduli and of the cell fluctuation allowance. In this respect, we underline that the form of Eq. (9) allows to avoid cell shrinking regardless of the specific choice of the λ-coefficients, an artifact that is often present in traditional CPM approaches. In this regard, some authors interpret the possible vanishing of cells due to specific parameter settings as the model counterpart of pressure-driven apoptosis [47] and delamination [66]. As shown by the simulations in Figs. 3 and 4, it is also evident that variations of the most relevant parameters of our node-based approach give rise to expected cell dynamics, i.e., coherent with those obtained from the traditional CPM. However, a more complete sensitivity analysis (as the one performed in [61]) would be needed to ensure that the evolution of the simulated system is consistent across a large range of parameter values and to allow researchers to qualitatively predict the model outcomes resulting from different regions of the parameter space. It is finally useful to remark that a proper fitting between the algorithm basic step and the actual time units is even more difficult. A good option is to employ an *a posteriori* calibration between selected quantities resulting from numerical outcomes and relevant and available experimental data. For example, is is consistent to fix the spatial unit of the computational domain and then to infer a reasonable relationships between a MCS and a proper temporal unit by comparing, e.g., cell velocity or the diffusive behavior of a chemical substance as evaluated either in model simulations or in experimental settings. Such a procedure is typically performed also in traditional CPM works [67, 90].

Since a powerful modeling approach should be able to adapt to different biological contexts and to describe multiple types of phenomena, we have illustrated also a sample simulation of a cell chemotactic migration. In this respect, we recall that directional components in cell motion are included in a number of CPMs. In most cases, they amount to chemotactic or durotactic energy contributions (similarly to Eq. (13)), which model the fact that cells crawl towards increasing gradients of soluble or insoluble chemical substances [68, 91, 106]. Further, some authors introduce a term in the Hamiltonian implementing a cell-shape dependent inertial movement (i.e., *persistence*). Such an energy contribution is typically expressed as a motile force, whose direction is determined by a feedback from the cell earlier displacements. It is involved both in single cell migration within three-dimensional matrix environments [94] and in the collective movement of dense cell monolayers [52]. In all these cases, a constant gradient in the energy functionals leads to a constant cell velocity, which results in an effective viscous friction between the cells and the extracellular substrate, at least for the range of parameter values used. Notably, the work by Kabla [52] shows that minute variations of cellular and environmental properties trigger transitions between well-defined multicellular migratory behavior (e.g., epithelial migration vs. mesenchymal movement, coordinated vs. disordered cell motion, collective vs. individual invasion).

As it possible to observe from the sample simulations shown in Section 3, the proposed node-based cell representation has some other advantages and disadvantages with respect to the pixel-based one of the traditional CPM. On one hand, it allows a direct matching between the simulated cell perimeter (i.e., surface in 3D) and the experimental counterpart: a reasonable correspondence is instead harder to be obtained with traditional CPMs. In these cases, as commented in [61], it is not possible to simply measure the total edge length between neighbouring lattice sites belonging to different cells. Large grid effects in fact emerge, with diagonally oriented edges presenting a significantly larger length than horizontally or vertically oriented edges [64]. Such an artifact is typically overcome by CPM authors by multiplying cell perimeter by a proper factor, see again [61] and references therein. Further, the proposed approach allows to describe extended cell membrane protrusions (e.g., filopodia and pseudopodia) more easily than the traditional CPM. Significantly long and thin cell structures are in fact typically obtained in classical pixel-based CPMs either by *a priori* assumptions on the target measure of selected cell axes [69] or by an unrealistical compartmentalization, such as the subdivision of cells into strings [99] or into sets of undifferentiated hexagonal subunits [65]. On the other side, each piece of cell membrane is represented in our model by a rigid segment connecting two consecutive nodes (in the absence of more complicated assumptions): this results in a decreased realism of the simulation outcomes, especially in the case of phenomena involving complex cell morphological transitions. Such a drawback can be partially avoided by cell node addition procedures, employed according to the problem of interest, as also commented in the text. Finally, a significant issue of our method is represented by the matching between the membranes of adherent cells. In fact, the distance between the nodes (and therefore between the edges) of a pair of cells in contact is equal to the characteristic size of the domain grid elements. In this respect, we suggest the researchers to perform a preliminary study of the system they want to simulate, in order to decide the optimal spatial resolution. However, they have to take into account that, as shown in the plot in Fig. 6 (C), reasonable increments in the mesh refinement do not affect the algorithm efficiency (at least in the case of fixed grids).

5.1. Comparison with vertex-based models

As seen in the previous part of the discussion, the CPM approach can be considered a member of the Cell Surface Mechanics models (CSMs). Our version of the CPM is even closer to such type of computational methods, and in particular to the subfamily of vertex-based models (VBMs). For the sake of completeness, we indeed propose a digression on VBMs, focused on their main features as well on a comparison with our node-based CPM.

The origins of VBMs relies in the study of inorganic structures such as soap bubbles [63], foams [77], and grain boundaries [54]. However, in the last decades such approaches are extensively used to investigate the biophysical mechanics underlying the deformation of epithelial tissues. The simple epithelium is a cell monolayer, composed of a dense population of strongly adhering cells, which are indeed densely packed and normally exhibit quasi-hexagonal shapes. The organization of epithelial sheets is mainly determined by selected cell properties, particularly remodeling ability and contact strength. Most vertex models represent either a cross-section or the apical surface of an epithelial sheet [36]. These simplifications allow to treat the component cells as two-dimensional elements, thereby reducing the computational complexity. Entering in more details, VBMs typically represent each cell as a polygon, with vertices and edges shared between adjacent individuals. This is the first relevant difference with respect to our model, where cell nodes and membrane segments belong to each single discrete element. In vertex models, the evolution of the shape and the position of the epithelial cells is largely due to the displacement of their vertices, which obey deterministic rules of motion (i.e., stochasticity is neglected as a consequence of the strong intercellular interactions). In particular, two further assumptions are usually done: each vertex is embedded in a viscous medium that applies a drag force and inertia can be neglected [36]. VBMs also incorporate procedures for junctional rearrangements, that allow cells to form and break bonds and be prevented from (self) intersecting. As described in [36] (cf. Fig. 3), in a cell neighbour exchange (also called T1 transition) two vertices sharing a short edge first merge into a single junction and then decompose into two different vertices. Further, a T2 transition consists in the removal of a cell characterized by a sufficiently small area. Finally, a T3 transition involves vertex/edge merging, which may be implemented in the case of epithelial sheets with voids and moving boundaries to avoid vertex/edge intersections [36].

As commented again in [36], one difference among vertex models relies in the fact that the forces acting on each vertex can be given explicitly (requiring indeed the solution of an equation of motion for each cell-cell junction) or through an energy minimization, similarly to CPM approaches. For instance, a series of models by Weliky and coworkers employs an explicit force-based approach, where the force on each cell vertex is given both by surface tensions and by a cortical pressure, The formers act in the direction of the cell membrane and are proportional to the perimeter of the interface, while the latter is the difference between the osmotic pressure tending to expand the cytoplasm and the restraining elastic pressure generated by the actin polymer fibers [110, 111]. These models are used to reproduce the key features of epiboly, i.e., coordinated cell movement involved in the gastrulation of the teleost fish Fundulus heterclitus [110], as well as to show that contact inhibition of cell motility and polarized protrusive activity are required to recapitulate normal notochord development in the African frog Xenopus laevis [111]. A variation of the above-described approaches is employed in the models by Brodland and co-workers, which are based on a finite element method. The authors first assume that the forces acting at each cell vertex are directed along the plasma membrane: further, they place an additional vertex at each cell centroid, which allows to create a proper triangulation suitable for their finite element formulation [11, 12, 13, 14, 15, 16, 17, 18, 19]. The models by the group of Brodland are then applied to study the biophysics of cell sorting and engulfment during embryogenesis. We here remark that an analysis focused on the relationship between cytoskeletal mechanics and cell behavior could be in principle performed also with our node-based approach. Differently to the traditional CPM, it is in fact more suitable to be interfaced with finite element methods, given the possibility of employing selected types of domain discretization.

Some of the most relevant studies using an energy-based approach are instead conducted by Honda and coworkers, who investigate how epithelial cells undergoing mechanical relaxation and neighbor exchange processes minimize their surface area while retaining a constant volume [48, 49, 50, 51]. An energy-based model is also set up by Farhadifar and colleagues, and extensively used to describe wing disk development in Drosophila [34]. In particular, the employed energy functional is very similar to the Hamiltonians presented in this work. It in fact reads as:

$$E = \sum_{\alpha} \frac{K_\alpha}{2}(A_\alpha - A_\alpha^0)^2 + \sum_{i,j} \Lambda_{ij} l_{ij} + \frac{\Gamma_\alpha}{2} L_\alpha^2, \tag{20}$$

where, given that α indicates each cell and (i, j) a pair of neighboring cell vertices belonging to different individuals, the first term is an elastic area constraint implementing intracellular pressure, the second summation models cell-cell adhesion (i.e., l_{ij} is the length of the membrane edge defined by vertices i and j) and the third term is the counterpart of the above-described cortical tension. The authors also include in their method a randomized cell division, and T1 and T2 transitions. They then study how cell mechanics and mitosis affect geometry and morphology (in terms of cell polygon number and of the relationship between cell area and perimeter) of the Drosophila wing disks. In particular, Farhadifar and coworkers estimate the values of key model parameters by comparing simulation outcomes and experimental results on the movement of the junctional network after laser ablation of individual cell boundaries. Later, Staple and colleagues undertake a systematic analysis of the ground states of the Farhadifar's vertex model, which correspond to the absolute minima of the energy function (20) for a given number of cells. In particular, a phase diagram is obtained, which determines the correspondence between selected regions of the parameter space and different types of ground states.

As elegantly commented in [36], force-based vertex approaches are more appropriate for dynamic systems sufficiently far from mechanical equilibrium or for those where the acting forces are well characterized. On the opposite, energy-based methods are more intuitive in the case of systems relaxing towards equilibrium or for those in which nonlocal effects are significantly involved.

Further comments are then needed on the implementation of cell division in vertex-based models. It is usually assumed that a cell splits into two individuals of equal area [11]. This can be accomplished with the determination of a specific dividing line and the subsequent addition of two new cell vertices where such a mitotic segment intersects the parent cell perimeter. The direction of the dividing line (i.e., of the angle of mitosis) may be taken from a uniform distribution (in the case of isotropic cell division), may be aligned to the shorter cell axis [13, 51], or may account of cell polarity [80]. The choice of division plane orientation can have a significant effect on the resulting epithelial sheet topology, and in particular on the frequency of hexagonal cells within the tissue [60]. As in the case of CPMs, the time of cell proliferation can be assumed in VBMs to occur stochastically [34] or to be determined by a detailed description of the cell cycle, which may account of cell growth and of a characteristic dormant period between mitotic events [104, 80]. It is however useful to comment that the above-described procedures to reproduce cell duplication mechanisms closely resemble the implementation proposed for our node-based model, sketched in Fig. 2 (A) and described in the relative part of text.

Vertex models can be easily modified to incorporate molecular dynamics. For instance, Smith and colleagues use in [96] an arbitrary Lagrangian-Eulerian formulation and a finite element method and couple the numerical solution of the reaction-diffusion equations governing morphogen and a vertex-based approach for epithelial reorganization, very similarly to our CPM. In particular, these authors assume that the rate of cell growth linearly increases with the local concentration of the given chemical substance. Schilling and coworkers instead employ and modify the energy-based model by Farhadifar in the context of the cell sorting at the anterior/posterior boundary in the Drosophila wing primordium [89]. They assume that the bond tensions Λ_{ij} in Eq. (20) depend on the local intracellular concentration of a putative molecule of the Hedgehog (Hh) signaling pathway. Further, they implement a finite volume method, typical of computational fluid dynamics, to solve the reaction-diffusion equations governing the Hh biochemical cascade. The approach by Schilling and colleagues can be considered *nested*, i.e., the microscopic/molecular scale affects mesoscopic cell behavior, similarly to what can be done in CPM approaches [92, 93].

The inclusion of mechanical aspects, as seen a fundamental improvement of our model with respect to traditional CPMs, can be also employed in vertex-based models. The pioneering work of Odell and coworkers uses a vertex model to study active or passive mechanical forces lead to tissue deformation [75, 76]. In particular, the authors represent a cross section of an embryo as a ring of cells: each of them is in turn defined by four interconnecting vertices subjected to a viscoelastic force. The apical edges also actively contract in response to stretch. Similar approaches examine the mechanics underlying tissue deformation in other systems, including the process of invagination of the optic cup in vertebrates [74, 85]. A model for the highly ordered packing of cells in the zebrafish retina [87] instead includes both mechanical and biochemical aspects in a vertex-based framework. In particular, the localization of planar cell polarity (PCP) proteins determines cell membrane edge tension, which mechanically affect cell and tissue geometry. Tissue organization and remodeling in turn constraint PCP distribution within each cell or between neighboring individuals. The resulting model outcomes suggest that cell patterning in the zebrafish adult retina requires the intervention of an externally applied force, representing intraocular pressure, and the progressive growth and division of cells exhibiting selected amounts of PCP. The model further predicts that cone mosaic defects arise from mechanical perturbations, as confirmed by experimental observations in bugeye mutant fish. Similarly, a model of wing imaginal disk size regulation, developed by Aegerter-Wilmsen and coworkers, assumes that cell cycle progression is modulated by the concentrations of key proteins associated with mechanotransduction and morphogen signaling [3]. In particular, these authors use a coupled set of differential algebraic equations to describe morphogen and selected cell-cell signaling pathways and a classical vertex model to represent cell growth, division, and remodeling. Cell mechanical compression then modulates the activity of selected proteins in the regulatory network which in turn affects the rate at which cells progress through the cell cycle and biases the direction of cell division. The model is finally able to reproduce a number of experimental observations, including the spatially uniform and non-uniform growth patterns in disks.

It is useful to notice that in most vertex-based models each cell junction is typically shared by a maximum of three cells, within the plane of the epithelial tissue, although four individuals may briefly meet as an intermediate state during a T1 transition. However, in some developmental processes a prominent event is the formation of multicellular clusters, where more than three cells share a common vertex. In this respect, Trichas and coworkers [104] employ a force-based approach similar to the already-cited models [110, 111] to analyze the functional importance of rosettes formation in the migration of the mouse anterior visceral endoderm (AVE). The AVE consists of a small group of specialized cells within the overall mouse visceral endoderm (VE). During AVE migration, the VE maintains integrity as an epithelial monolayer, and the portion of the VE through which the AVE migrates undergoes significant intercalation and dynamic change in cell organization [98, 105]. To allow for rosette formation, the authors implement simple T1 transitions as well as vertex/vertex merge operations, which occur when a cell edge length falls below a given threshold, whose value is demonstrated to affect the resulting pattern. We here remark that rosette formation processes can be easily captured by our version of the CPM. In fact, a given membrane node i of a cell c, placed in grid vertex $\mathbf{x}_j$, can be surrounded by a number of nodes belonging to different individuals equal to the number of grid vertices forming its neighborhood $\overline{\Omega}_j$. For instance, in the case of the domain discretization proposed in Fig. 1 (B), a cell can have contact interactions even with six other individuals.

The vertex-based approaches reviewed so far are characterized by an essentially two-dimensional nature. However, Osterfield and coworkers adapt and modify the model by Farhadifar to study the 3D formation of the dorsal appendices of Drosophila eggshell [78]. In particular, they allow two-dimensional cell sheets to move freely in three-dimensional space. This work is also based on selected experimentally hypothesis on the patterns of tension within the apical surface of the follicular epithelium. A more realistic approach to model of three-dimensional morphogenesis consists in representing cells as prisms, rather than as flat polygons, as done by Honda and coworkers to study the emergence of geometric asymmetries in the mouse blastocyst [48, 49] and to point out the mechanisms underlying cell intercalation in spherical shells [50]. Three-dimensional dynamics can in principle be reproduced also by our node-based CPM, which can be employed in 3D domains. Such an extension requires the redefinition of the neighborhood set of the grid vertices and the implementation of new procedures to calculate cell geometrical attributes (e.g., surface and volume). Specific rules for cell node addition/removal and for cell duplication have to be given as well.

One of the fundamental problems at the basis of vertex models is surface rearrangement upon energy minimization and constraints. This issue is the focus of the interactive program Surface Evolver [8], which uses a finite element method to represent a surface as a union of simplices. In particular, each facet is defined by a chain of three oriented edges, which are in turn defined by a pair of ordered vertices. This permits the representation of surfaces characterized by complicated topology. Finally, 3D bodies can be defined by a list of oriented facets, that make up their boundary. In this respect, tt is not necessary to have a simplicial decomposition of the interior bulk of a body, since the Surface Evolver works on 2D elements, eventually embedded in the 3D space. The energy, whose minimization drives surface rearrangements (similarly to our node-based model) can be a combination of tensions, gravitational potentials, and of any other energy contribution that can be expressed as an integral over an area. The set of constraints instead involves vertices, edges and bodies. For instance, a vertex may be fixed in place or constrained to lie on a smooth manifold. A body may be instead forced to have a fixed volume. A method for energy minimization is finally needed, as the Metropolis algorithm typical of CPMs. Several operations are also available for manipulating the finite element triangulation, which include refinements (i.e., subdivision of each facet into four similar facets for better approximation of curved surfaces), equiangulation (i.e., readjustment of the triangulation to make surface facets as nearly equilateral as possible), or vertex averaging (shifts of a vertex to the average position of its neighbors). Some of the applications of the Surface Evolver package include the modeling of the shape of fuel in rocket tanks in low gravity situations [103], the calculation of areas for the opaque cube problem [9], and the study of grain boundaries [10].

A member of the group of CSM approaches is also the model by Newman [73], where cell vertices are used to represent cytoskeletal elements forming the entire cell body (and not only to define cell membranes, as in most VBMs and in the case of our node-based CPM). The dynamics of such subcellular elements are then determined by the solution of Langevin equations, which account for a weak stochastic component (i.e., mimicking cytoplasmic fluctuations) and selected elastic responses to both intracellular and intercellular biomechanical forces (all modeled by generalized Morse potentials).

5.2. Conclusions

This paper is intended as a foundational work presenting a different version of the cellular Potts model. In particular, we think at our node-based method as an alternative approach to deal with biological and biomedical problems. As explained in the comments on the simulation outcomes, and deeply discussed in this last section, it has in fact advantages and disadvantages with respect both to the traditional CPM and to vertex-based models. The choice of using our method may be determined by the phenomenon of interest. For instance, the collective migratory behavior characterizing many types of confluent monolayers can be better described by a vertex-based approach. However, VBMs can hardly deal with the evolution of systems where cells detach from neighboring individuals (e.g., tumor growth and invasion) or where network-like patterns emerge (e.g., vascular progression). On the other hand, the traditional version of the CPM is preferable in the case of the evolution of systems formed by a large number of cells (due to the reduced computational complexity). In this respect, to achieve a reasonable competitiveness of our model, it is necessary an algorithm optimization and the subsequent test application to more realistic biological scenarios.

[1] Alber MS, Kiskowski MA, Glazier JA, Jiang Y. On cellular automation approaches to modeling biological cells. In Mathematical Systems Theory in Bi- ology, Communication and Finance (eds. J Rosenthal and DS Gilliam), Springer-Verlag, New York, 1 – 40, 2004.

[2] Cell Mechanics: From Single Scaled-Based Models to Multscale Modeling (eds. A Chauviere, L Preziosi, and C Verdier), Mathematical and Computational Biology Series. Chapman Hall/CRC Press, London, 2010.

[3] Aegerter-Wilmsen T, Heimlicher MB, Smith AC, de Reuille PB, Smith RS, Aegerter CM, Basler K. Integrating force-sensing and signaling pathways in a model for the regulation of wing imaginal disc size. Development, 2012; 139: 3221 – 3231.

[4] Armstrong PB, Parenti D. Cell sorting in the presence of cytochalasin b. J Cell Biol, 1972; 55: 542 - 553.

[5] Balter A, Merks RMH, Poplawski NJ, Swat M, Glazier JA. The Glazier-Graner-Hogeweg model: Extensions, future directions, and opportunities for further study. In Single-Cell-Based Models in Biology and Medicine (eds. ARA Anderson, MAJ Chaplain, and KA Rejniak), Mathematics and Biosciences in Interactions, Birkaüser, Basel, 151 - 167, 2007.

[6] Bardet PL, Guirao B, Paoletti C, Serman F, Lopold V, Bosveld F, Goya Y, Mirouse V, Graner F, Bellaïche Y. PTEN controls junction lengthening and stability during cell rearrangement in epithelial tissue. Dev Cell, 2013; 25: 534 – 546.

[7] Bortz AB, Kalos MH, Lebowitz JL. A new algorithm for Monte Carlo simulation of Ising spin systems. J Comp Phys, 1975; 17: 10 – 18.

[8] Brakke KA. The Surface Evolver. Experiment Math, 1992; 1: 141 – 165.

[9] Brakke KA. The opaque cube problem. In Computing Optimal Geometries (video and booklet, ed. JE Taylor), American Mathematical Society, Providence, 1991.

[10] Brakke KA. Grain growth with the Surface Evolver. In Video Proceedings of the Workshop on Computational Crystal Growing (ed. JE Taylor), American Mathematical Society, Providence, 1992.

[11] Brodland GW. Computational modeling of cell sorting, tissue engulfment, and related phenomena: a review. Appl Mech Rev, 2004; 57: 47 - 76.

[12] Brodland GW. The differential interfacial tension hypothesis (DITH): a comprehensive theory for the self-rearrangement of embryonic cells and tissues. J Biomech Eng, 2002; 124: 188 - 197.

[13] Brodland GW, Veldhuis JH. Computer simulations of mitosis and interdependencies between mitosis orientation, cell shape and epithelia reshaping. J Biomech, 2002; 35: 673 - 681.

[14] Brodland GW, Chen DIL, Veldhuis JH. A cell-based constitutive model for embryonic epithelia and other planar aggregates of biological cells. Int J Plast, 2006; 22: 965 - 995.

[15] Brodland GW, Yang J, Sweny J. Cellular interfacial and surface tensions determined from aggregate compression tests using a finite element model. HFSP J, 2009; 3: 273 - 281.

[16] Brodland GW, Clausi DA. Embryonic tissue morphogenesis modeled by FEM. J Biomech Eng, 1994; 116: 146 - 155.

[17] Brodland GW. Finite element methods for developmental biology. Int Rev Cytol, 1994; 150: 95- 118.

[18] Brodland GW, Wiebe CJ. Mechanical effects of cell anisotropy on epithelia. Comput Methods Biomech Biomed Engin, 2004 7: 91- 99.

[19] Brodland GW, Viens D, Veldhuis JH.A new cell-based FE model for the mechanics of embryonic epithelia. Comput Methods Biomech Biomed Engin, 2007; 10: 121 - 128.

[20] Cavallaro U, Christofori G. Cell adhesion in tumor invasion and metastasis: Loss of the glue is not enough. Biochim Biophys Acta, 2001; 1552: 39 – 45.

[21] Cavallaro U, Christofori G. Cell adhesion and signalling by cadherins and Ig-CAMs in cancer. Nat Rev Cancer, 2004; 4: 118 – 132.

[22] Cercato FP, Mombach JC, Cavalheiro GG. High performance simulations of the cellular Potts model. 20th International Symposium on High-Performance Computing in an Advanced Collabo- rative Environment, 28, 2006.

[23] Chaturvedi R, Huang C, Izaguirre JA, Newman SA, Glazier JA, Alber MS. A hybrid discrete-continuum model for 3- D skeletogenesis of the vertebrate limb. Lect Notes Comput Sci, 2004; 3305: 543 – 552.

[24] Chen N, Glazier JA, Izaguirre JA, Alber MS. A parallel implementation of the cellular Potts model for simulation of cell-based morphogenesis. Comput Phys Commun, 2007; 176: 670 – 681.

[25] Chichilnisky EJ. A mathematical model for patternf formation. J Theor Biol, 1986; 123: 81 - 101.

[26] Christofori G. Changing neighbours, changing behaviour: cell adhesion molecule-mediated signalling during tumour progression. EMBO J, 2003; 22: 2318 – 2323.

[27] Classen AK, Anderson KI, Marois E, Eaton S. Hexagonal packing of Drosophila wing epithelial cells by the planar cell polarity pathway. Dev Cell, 2005; 9: 805 - 817.

[28] Dallon JC, Scott M, Smith WV. A force based model of individual cell migration with discrete attachment sites and random switching terms. Journal of Biomechanical Engineering, 2013; 135: 71008.

[29] Dallon JC, Evans EJ, Grant CP, Smith WV. Cell speed is independent of force in a mathematical model of amoeboidal cell motion with random switching terms. Mathematical Biosciences, 2013; 247: 1 – 7.

[30] Dan D, Mueller C, Chen K, Glazier JA. Solving the advection-diffusion equations in biological contexts using the cellular Potts model. Phys Rev E Stat Nonlin Soft Matter Phys, 2005; 72: 041909.

[31] Dhatt G, Lefrançois E, Touzot G. Finite Element Method, John Wiley & Sons, Hoboken, 2012.

[32] De Beco S, Amblard S, Coscoy S. New insights into the regulation of E-cadherin distribution by endocytosis. In International Review of Cell and Molecular Biology (ed. KW Jeon), Academic Press, Burlington, 63 – 108, 2012.

[33] Drasdo D. On selected individual-based approaches to the dynamics of multicellular systems. In Multiscale Modeling (eds. W Alt and M Griebel), Birkaüser, Basel, 169 – 203, 2005.

[34] Farhadifar R, Röper JC, Aigouy B, Eaton S, Jülicher F. The influence of cell mechanics, cell-cell interactions, and proliferation on epithelial packing. Curr Biol, 2007; 17: 2095 – 2104.

[35] Fichthorn KA, Weinberg WH. Theoretical foundations of dynamical Monte Carlo simulations. J Chem Phys, 1991; 95: 1090 – 1096.

[36] Fletcher AG, Osterfield M, Baker RE, Shvartsman SY. Vertex models of epithelial morphogenesis. Biophys J, 2014; 106: 2291 – 2304.

[37] Franco C, Tzvetkova–Chevolleau T, Stéphanou A. On the influence of discrete adhesive patterns for cell shape and motility: a computational approach. Math Model Nat Phenon, 2010; 5: 56 – 83.

[38] Gamba A, Ambrosi D, Coniglio A, De Candia A, Di Talia S, Giraudo E, Serini G, Preziosi L, Bussolino F. Percolation, morphogenesis, and Burgers dynamics in blood vessel formation. Phys Rev Letters, 2003; 90: 101 – 118.

[39] Gibson MC, Patel AB, Nagpal R, Perrimon N. The emergence of geometric order in proliferating metazoan epithelia. Nature, 2006; 442: 1038 - 1041.

[40] Glazier JA, Graner F. Simulation of the differential adhesion driven rearrangement of biological cells. Physical Rev E, 1993, 47: 2128 – 2154.

[41] Glazier JA, Balter A, Merks RMH, Poplawski NJ, Swat M. The Glazier-Graner-Hogeweg model: Extension, future direction, and opportunitites for further study. In Single Cell-Based Models in Biology and Medicine (eds. ARA Anderson, MAJ Chaplain, and KA Rejniak), Mathematics and Biosciences in Interactions, Birkaüser, Basel, 157 - 167, 2007.

[42] Glazier JA, Balter A, Poplawski NJ. Magnetization to morphogenesis: A brief history of the Glazier-graner-Hogeweg model. In Single Cell-Based Models in Biology and Medicine (eds. ARA Anderson, MAJ Chaplain, and KA Rejniak), Mathematics and Biosciences in Interactions, Birkaüser, Basel, 79 - 106, 2007.

[43] Graner F, Glazier JA. Simulation of biological cell sorting using a two-dimensional extended Potts model. Phys Rev Lett, 1992; 69: 2013 – 2017.

[44] Green JBA. Sophistications of cell sorting. Nat Cell Biol, 2008; 10: 375 – 377.

[45] Gusatto E, Mombach JC, Cercato FP, Cavalheiro GH. An efficient parallel algorithm to evolve simulations of the cellular Potts model. Parallel Processing Letters, 2005; 15:199 – 208.

[46] Harris AK. Is cell sorting caused by differences in the work of intercellular adhesion? A critique of the Steinberg hypothesis. J Theor Biol 1976; 61, 267 – 285.

[47] Hogeweg P. Evolving mechanisms of morphogenesis: on the interplay between differential adhesion and cell differentiation. J Theor Biol, 2000; 203: 317 - 333.

[48] Honda H, Motosugi N, Nagai T, Tanemura M, Hiiragi T. Computer simulation of emerging asymmetry in the mouse blastocyst. Development, 2008; 135: 1407 – 1414.

[49] Honda H, Tanemura M, Nagai T. A three-dimensional vertex dynamics cell model of space-filling polyhedra simulating cell behavior in a cell aggregate. J Theor Biol, 2004; 226: 439 - 453.

[50] Honda H, Nagai T, Tanemura M. Two different mechanisms of planar cell intercalation leading to tissue elongation. Dev Dyn, 2008; 237: 1826 - 1836.

[51] Honda H, Yamanaka H, Eguchi G. Transformation of a polygonal cellular pattern during sexual maturation of the avian oviduct epithelium: computer simulation. J Embryol Exp Morphol, 1986; 98: 1 - 19.

[52] Kabla AJ Collective cell migration: leadership, invasion and segregation. J R Soc Interface, 2012; 9: 3268 – 3278.

[53] Käfer J, Hayashi T, Marée AF, Carthew RW, Graner F. Cell adhesion and cortex contractility determine cell patterning in the Drosophila retina. Proc Natl Acad Sci USA, 2007; 104: 18549 - 18554.

[54] Kawasaki K, Nagai T, Nakashima K. Vertex models for two-dimensional grain growth. Philos Mag B, 1989; 60: 399 - 421.

[55] Korniss G, Novotny MA, Rikvold PA. Parallelization of a dynamic Monte Carlo algorithm: a partially rejection-free conservative approach. Journal of Computational Physics, 1999; 153: 488.

[56] Kovacs EM, Yap AS. Cell-cell contact: cooperating clusters of actin and cadherin. Curr Biol, 2008; 18: R667 – R669.

[57] Krieg M, Arboleda-Estudillo Y, Puech PH, Käfer J, Graner F, Müller DJ, Heisenberg CP. Tensile forces govern germ-layer organization in zebrafish. Nat Cell Biol, 2008; 10: 429 – 436.

[58] Lecuit T, Lenne PF. Cell surface mechanics and the control of cell shape, tissue patterns and morphogenesis. Nat Rev Mol Cell Biol, 2007; 8: 633 - 644.

[59] Lee KC. Rejection-free Monte Carlo technique. J Phys A, 1995; 28: 4835.

[60] Li Y, Naveed H, Kachalo S, Xu LX, Liang J. Mechanisms of regulating cell topology in proliferating epithelia: impact of division plane, mechanical forces, and cell memory. PLoS One, 2012; 7: e43108.

[61] Magno R, Grieneisen VA, Marée AFM. The biophysical nature of cells: potential cell behaviours revealed by analytical and computational studies of cell surface mechanics BMC Biophysics, 2015; 8: 8.

[62] Manning ML, Foty RA, Steinberg MS, Schoetz EM. Coaction of intercellular adhesion and cortical tension specifies tissue surface tension. Proc Nat Acad Sci USA, 2010; 107: 12517 - 12522.

[63] Marder M. Soap-bubble growth. Phys Rev A, 1987; 36: 438 - 440.

[64] Marée AFM, Grieneisen VA, Hogeweg P. The Cellular Potts Model and biophysical properties of cells, tissues and morphogenesis In Single Cell-Based Models in Biology and Medicine (eds. ARA Anderson, MAJ Chaplain, and KA Rejniak), Mathematics and Biosciences in Interactions, Birkaüser, Basel, 107 - 136, 2007.

[65] Marée AFM, Jilkine A, Dawes A, Grieneisen VA, Edelstein-Keshet L. Polarization and movement of keratocytes: A multiscale modelling approach. Bull Math Biol, 2006; 68: 1169 - 1211.

[66] Marinari E, Mehonic A, Curran S, Gale J, Duke T, Baum B. Live-cell delamination counterbalances epithelial growth to limit tissue overcrowding. Nature, 2012; 484: 542 - 545.

[67] Merks RMH, Koolwijk P. Modeling morphogenesis in silico and in vitro: Towards quantitative, predictive, cell-based modeling. Math Modell Nat Phenom, 2009; 4: 149 - 171.

[68] Merks RMH, Glazier JA. Dynamic mechanisms of blood vessel growth. Nonlinearity, 2006; 19: C1 – C10.

[69] Merks RMH, Glazier JA, Brodsky SV, Goligorksy MS, Newman SA. Cell elongation is key to in silico replication of in vitro vasculogenesis and subsequent remodeling. Dev Biol, 2006; 289: 44 – 54.

[70] Mombach JC, Glazier JA, Raphael RC, Zajac M. Quantitative comparison between differential adhesion models and cell sorting in the presence and absence of fluctuations. Phys Rev Lett, 1995; 75: 2244 – 2247.

[71] Montero E, Abreu C, Tonino P. Relationship between VEGF and p53 expression and tumor cell proliferation in human gastrointestinal carcinomas. J Cancer Res Clin Oncol, 2007; 134: 193 – 201.

[72] Narimatsu M, Bose R, Pye M, Zhang L, Miller B, Ching P, Sakuma R, Luga V, Roncari L, Attisano L, Wrana JL. Regulation of planar cell polarity by Smurf ubiquitin ligases. Cell, 2009; 137: 295 - 307.

[73] Newman TJ. Modeling multicellular systems using subcellular elements. Math Biosci Eng, 2005; 2: 613 – 624.

[74] Nishimura M, Inoue Y, Hayashi S. A wave of EGFR signaling determines cell alignment and intercalation in the Drosophila tracheal placode. Development, 2007; 134: 4273 - 4282.

[75] Odell GM, Oster G, Alberch P, Burnside B. The mechanical basis of morphogenesis. I. Epithelial folding and invagination. Dev Biol, 1981; 85: 446 – 462.

[76] Odell G, Oster G, Burnside B, Alberch P. A mechanical model for epithelial morphogenesis. J Math Biol, 1980; 9: 291 – 295.

[77] Okuzono T, Kawasaki, K. Intermittent flow behavior of random foams: a computer experiment on foam rheology. Phys Rev E Stat Phys Plasmas Fluids Relat Interdiscip Topics, 1995; 51: 1246 - 1253.

[78] Osterfield M, Du X, Schpbach T, Wieschaus E, Shvartsman SY. Three-dimensional epithelial morphogenesis in the developing Drosophila egg. Dev Cell, 2013; 24: 400 – 410.

[79] Ouchi NB, Glazier JA, Rieu JP, Upadhyaya A, Sawada Y. Improving the realism of the cellular Potts model in simulations of biological cells. Physica A, 2003; 329: 451 - 458.

[80] Patel AB, Gibson WT, Gibson MC, Nagpal R. Modeling and inferring cleavage patterns in proliferating epithelia. PLoS Comput Biol, 2009; 5: e1000412.

[81] Perryn ED, Czirok A, Little CD. Vascular sprout formation entails tissue deformations and VE-cadherin dependent cell-autonomous motility. Dev Biol, 2008; 313: 545 - 555.

[82] Poplawski NJ, Swat M, Gens JS, Glazier JA. Adhesion between cells, diffusion of growth factors, and elasticity of the AER produce the paddle shape of the chick limb. Physica A, 2007, 373: 521 – 532.

[83] Potts RB. Some generalized order-disorder transformations, Proc Cambridge Phil Soc, 1952; 48: 106 - 109.

[84] Purcell EM. Life at low Reynolds number. Am J Phys, 1977; 45: 3 - 11.

[85] Rauzi M, Hocevar Brezavscek A, Ziherl P, Leptin M. Physical models of mesoderm invagination in Drosophila embryo. Biophys J, 2013; 105:3 – 10.

[86] Rieu JP, Upadhyaya A, Glazier JA, Ouchi NB, Sawada Y. Diffusion and deformations of single Hydra cells in cellular aggregates. Biophys J, 2000; 79: 1903 - 1914.

[87] Salbreux G, Barthel LK, Raymond PA, Lubensky DK. Coupling mechanical deformations and planar cell polarity to create regular patterns in the zebrafish retina. PLoS Comput Biol, 2012; 8: e1002618.

[88] Savill NJ, Hogeweg P. Modelling morphogenesis: From single cells to crawling slugs. J Theor Biol, 1997; 184: 118 – 124.

[89] Schilling S, Willecke M, Aegerter-Wilmsen T, Cirpka OA, Basler K, von Mering C. Cell-sorting at the A/P boundary in the Drosophila wing primordium: a computational model to consolidate observed non-local effects of Hh signaling. PLoS Comput Biol, 2011; 7: e1002025.

[90] Scianna M. A multiscale hybrid model for pro-angiogenic calcium signals in a vascular endothelial cell. Bull Math Biol, 2011; 74: 1253 – 1291.

[91] Scianna M, Munaron L, Preziosi L. A multiscale hybrid approach for vasculogenesis and related potential blocking therapies. Prog Biophys Mol Biol, 2011; 106: 450 – 462.

[92] Scianna M, Preziosi L. Multiscale Developments of the Cellular Potts Model. Multiscale Model Simul, 2012; 10: 342 – 382.

[93] Scianna M, Preziosi L. Cellular Potts Models: Multiscale Developments and Biological Applications, Chapman & Hall/CRC Press, London, 2013.

[94] Scianna M, Preziosi L. Modeling the influence of nucleus elasticity on cell invasion in fiber networks and microchannels. J Theor Biol, 2013; 317: 394 – 406.

[95] Serini G, Ambrosi D, Giraudo E, Gamba A, Preziosi L, Bussolino F. Modeling the early stages of vascular network assembly. EMBO J, 2003; 22: 1771 - 1779.

[96] Smith AM, Baker RE, Kay D, Maini PK. Incorporating chemical signalling factors into cell-based models of growing epithelial tissues. J Math Biol, 2012; 65: 441– 63.

[97] Smith JA, Martin L.Do cells cycle? Proc Natl Acad Sci USA, 1973; 70: 1263 – 1267.

[98] Srinivas S, Rodriguez T, Clements M, Smith JC, Beddington RS. Active cell migration drives the unilateral movements of the anterior visceral endoderm. Development, 2004; 131: 1157 – 1164.

[99] Starruß J, Bley T, Søgaard-Andersen L, Deutsch A. A new mechanism for collective migration in Myxococcus Xanthus, J Stat Phys, 2007; 128: 269 - 286.

[100] Steele IA, Edmondson RJ, Leung HY, Davies BR. Ligands to FGF receptor 2-IIIb induce proliferation, motility, protection from cell death and cytoskeletal rearrangements in epithelial ovarian cancer cell lines. Growth Factors, 2006; 24: 45 – 53.

[101] Steinberg MS. Reconstruction of tissues by dissociated cells. Some morphogenetic tissue movements and the sorting out of embryonic cells may have a common explanation. Science, 1963; 141: 401 – 408.

[102] Steinberg MS. Does differential adhesion govern self-assembly processes in histogenesis? Equilibrium configurations and the emergence of a hierarchy among populations of embryonic cells. J Exp Zool, 1970; 173: 395 – 433.

[103] Tegart J. Three-dimensional fluid interfaces in cylindrical containers. AIAA paper AIAA-91-2174, 27th Joint Propulsion Conference, Sacramento, 1991.

[104] Trichas G, Smith AM, White N, Wilkins V, Watanabe T, Moore A, Joyce B, Sugnaseelan J, Rodriguez TA, Kay D, Baker RE, Maini PK, Srinivas S. Multicellular rosettes in the mouse visceral endoderm facilitate the ordered migration of anterior visceral endoderm cells. PLoS Biol, 2012; 10: e1001256.

[105] Trichas G, Joyce B, Crompton LA, Wilkins V, Clements M, Tada M, Rodriguez TA, Srinivas S.Nodal dependent differential localisation of dishevelled-2 demarcates regions of differing cell behaviour in the visceral endoderm. PLoS Biol, 2011; 9: e1001019.

[106] Turner S, Sherratt JA. Intercellular adhesion and cancer invasion: A discrete simulation using the extended Potts model. J Theor Biol, 2002; 216: 85 – 100.

[107] Voss-Böhme A. Multi-scale modeling in morphogenesis: A critical analysis of the cellular Potts model. PLoS ONE, 2012; 7: e42852.

[108] Wang N, Tytell JD, Ingber DE. Mechanotransduction at a distance: Mechanically coupling the extracellular matrix with the nucleus. Nat Rev Mol Cell Biol, 2009; 10: 75 – 82.

[109] Wolff T, Ready D. In The Development of Drosophila melanogaster (eds. M Bate and A Martinez Arias), Cold Spring Harbor Laboratory Press, Cold Spring Harbor, 1277 - 1325, 1993.

[110] Weliky M, Oster G. The mechanical basis of cell rearrangement. I. Epithelial morphogenesis during Fundulus epiboly. Development, 1990; 109: 373 - 386.

[111] Weliky M, Minsuk S, Keller R, Oster G. Notochord morphogenesis in Xenopus laevis: simulation of cell behavior underlying tissue convergence and extension. Development, 1991; 113: 1231 – 1244.

[112] Wright SA, Plimpton SJ, Swiler PT, Fye RM, Young MF, Holm EA. Potts-model grain growth simulations: Parallel algorithms and applications Sandia Report, pp. 1 - 47, 1997.

[113] Zhang Y, Vande Woude GF. HGF/SF-Met signaling in the control of branching morphogenesis and invasion. J Cell Biochem, 2003; 88: 408 – 417.

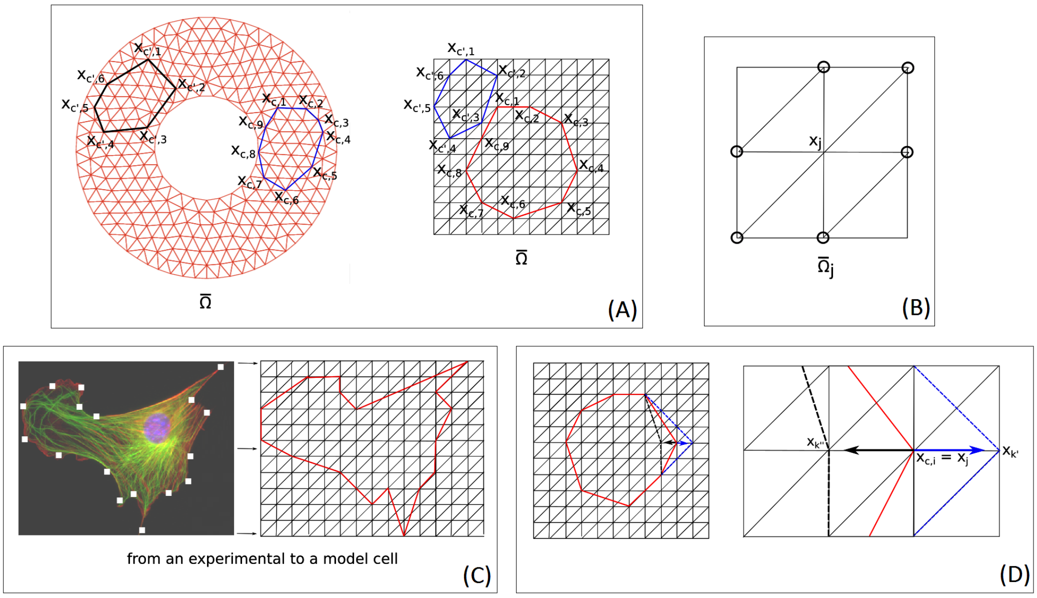
xc',1
xc',2
xc',3
xc',4
xc',5
xc',6
xc,1
xc,2
xc,3
xc,4
xc,5
xc,6
xc,7
xc,8
xc,9
Ω̄
(A)
xj
Ω̄j
(B)
from an experimental to a model cell
(C)
xk''
xc,i = xj
xk'
(D)

Figure 1: (A) Examples of 2D dicretized domains $\overline{\Omega}$ containing two representative cells, c (defined by V_c= 9 membrane nodes) and c' (defined by $V_{c'} = 6$ membrane nodes). (B) First-nearer neighborhood $\overline{\Omega}_j$ of a generic grid vertex j, which is composed of the set of manually encircled grid vertices. (C) Sample procedure to properly reproduce in the model a complex cell shape (see the text for details). (D) Basic Monte Carlo Step (MCS) of the Metropolis algorithm. A membrane node i of a cell c, which actually coincides with grid vertex j (i.e., $\mathbf{x}_{c,i}(t) = \mathbf{x}_j$) is selected at random and attempts move to one of the free neighboring grid vertex locations $\mathbf{x}_k \in \overline{\Omega}_j$. In particular, if the target grid vertex is within the cell (say, k''), c is retracting (see the dark-dashed line). Otherwise, if the target grid vertex is outside the cell (say, k'), c is protruding (see the blue-dashed line).

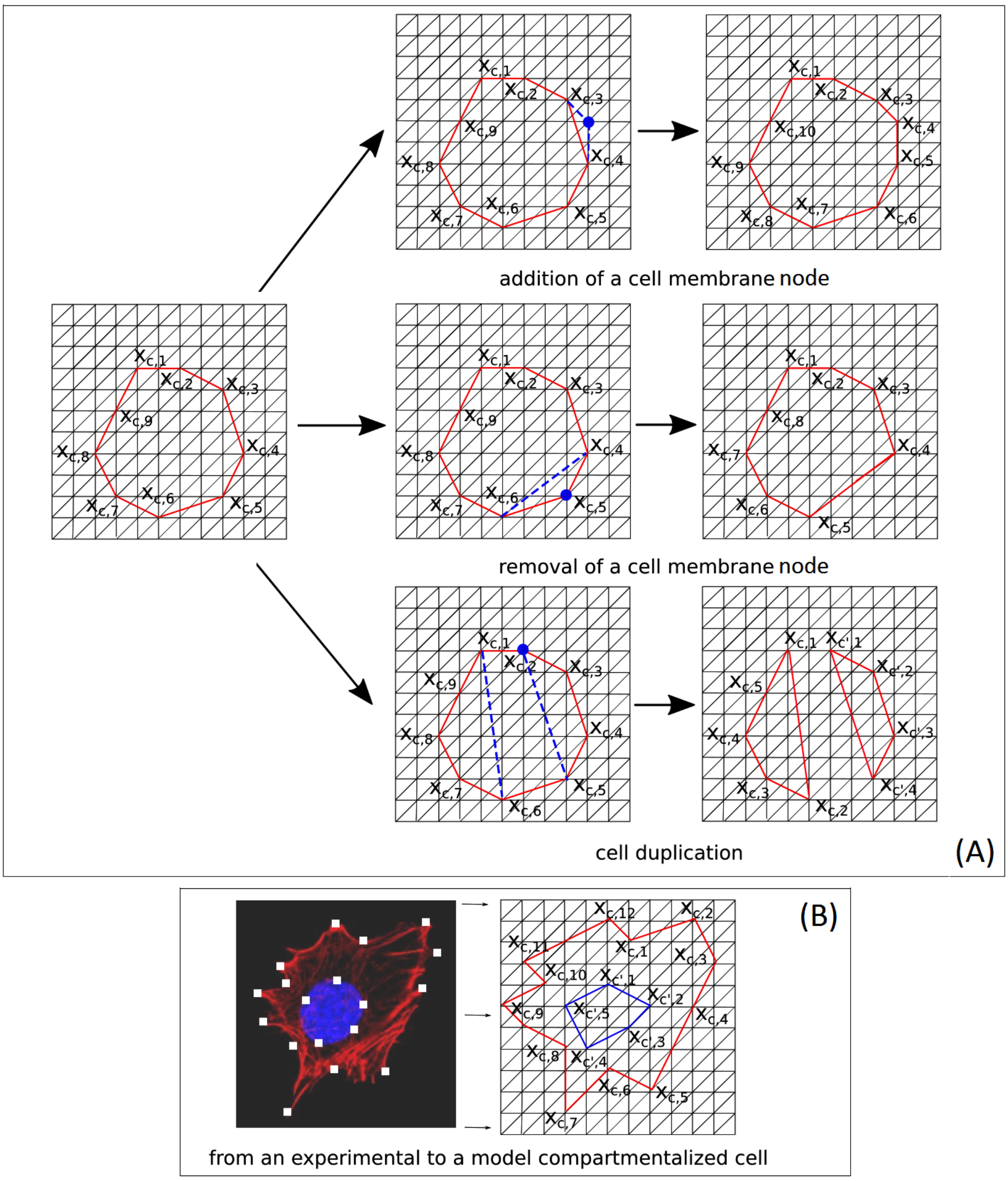

Xc,1
Xc,2
Xc,3
Xc,4
Xc,5
Xc,6
Xc,7
Xc,8
Xc,9
Xc,10
addition of a cell membrane node
removal of a cell membrane node
Xc',1
Xc',2
Xc',3
Xc',4
cell duplication
(A)
Xc,11
Xc,12
Xc',5
(B)
from an experimental to a model compartmentalized cell

Figure 2: (A) Sample procedures to model node addition/removal and cell duplication. The full blue dots indicate the cell nodes added/removed/selected to start division mechanisms. The dashed blue segments represent the cell membrane edges resulting from the process of interest. (B) Bi-compartmental cell, i.e., differentiated in the nucleus (c', with $V_{c'} = 5$ nodes) and in the cytosolic region (c, with $V_c = 12$ nodes).

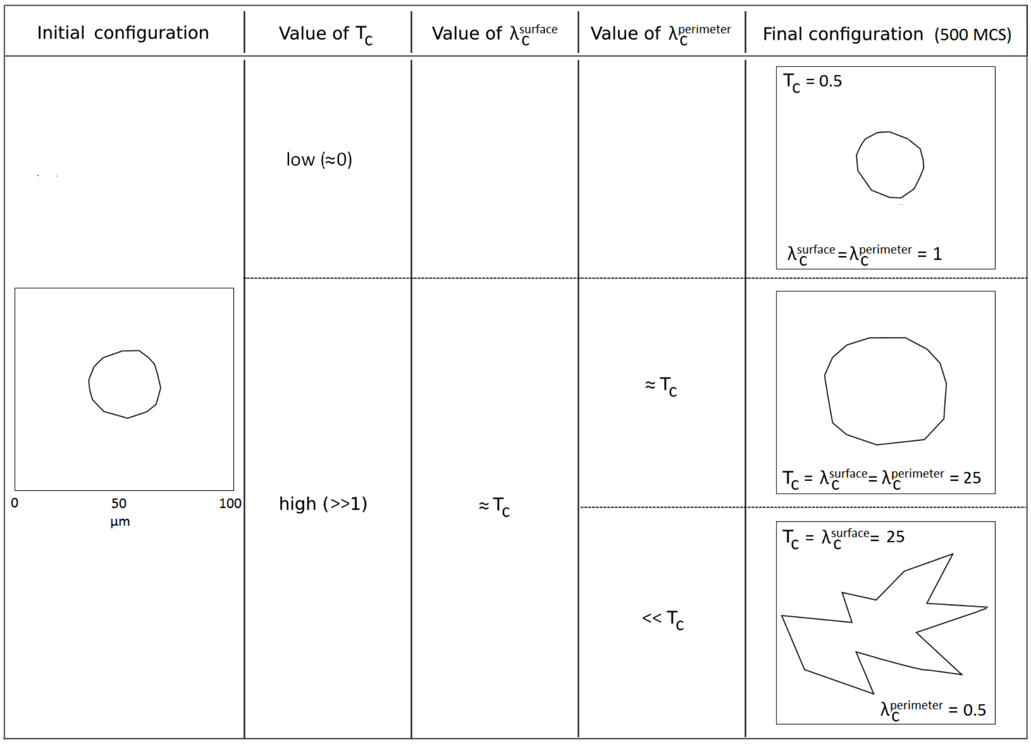
Initial configuration
Value of T_c
Value of λ_c^surface
Value of λ_c^perimeter
Final configuration (500 MCS)
low (≈0)
T_c = 0.5
λ_c^surface = λ_c^perimeter = 1
0
50
100
μm
high (>>1)
≈ T_c
≈ T_c
T_c = λ_c^surface = λ_c^perimeter = 25
<< T_c
T_c = λ_c^surface = 25
λ_c^perimeter = 0.5

Figure 3: Illustrative simulations of the biological role of the cell geometrical constraints in Eqs. (11a)-(11b). In a 100 μm $\times$ 100 μm domain Ω, an initially round cell $c = 1$, defined by 14 membrane nodes is placed. Its initial measures are equal to the half of the target dimensions. If the fluctuation allowance is low, the cell remains almost freezed. On the opposite, at high enough values of $T_{c=1}$, the cell stabilizes into an equilibrium configuration, given by the target measures, if both $\lambda_{c=1}^{\text{surface}}$ and $\lambda_{c=1}^{\text{perimeter}}$ fall within the same range (say, $= T_{c=1}$), whereas it continuously remodels while preserving its overall area if $\lambda_{c=1}^{\text{perimeter}} \ll \lambda_{c=1}^{\text{surface}} = T_{c=1}$. The specific parameter values used for each representative realization are included in the corresponding panel. In all cases, the simulation are run for 500 MCS.

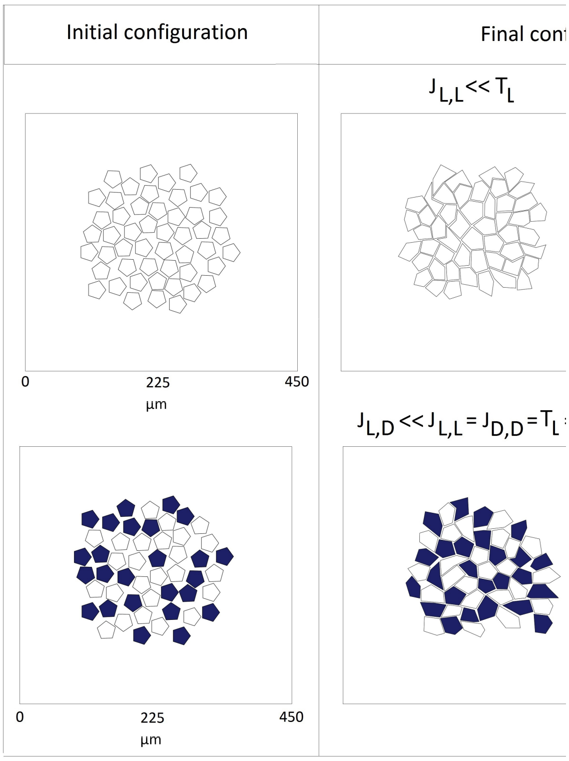

Figure 4: Illustrative simulations of the biological role of the adhesive energies. Top panels: in a 2.025×10^5 μm^2 domain Ω, an aggregate of 50 cells is placed. The cells are all of the same type: they are defined by 5 membrane nodes and have target and initial dimensions both equal to 60 μm and 300 μm^2, respectively. Further, we use the following parameter setting: $T_c = T_L = \lambda_c^{\text{surface}} = \lambda_L^{\text{surface}} = 25$, $\lambda_c^{\text{perimeter}} = \lambda_L^{\text{perimeter}} = 0.5 \ll T_L$, for all $c = 1, \dots, 50$. The final configurations (i.e., at 5000 MCS) correspond to $J_{L,L} = 0.5 \ll T_L$ and to $J_{L,L} = 25 = T_L$, respectively. Bottom panels: in the same domain Ω, the cell aggregate is now formed by individuals of different types (i.e., dark and light). They however share all the biophysical properties, as $T_c = T_L = T_D = \lambda_c^{\text{surface}} = \lambda_L^{\text{surface}} = \lambda_D^{\text{surface}} = 25$, $\lambda_c^{\text{perimeter}} = \lambda_L^{\text{perimeter}} = \lambda_D^{\text{perimeter}} = 0.5 \ll T_L = T_D$, for all $c = 1, \dots, 50$, and initial/target dimensions. The final configurations (i.e., at 5000 MCS) correspond to $J_{L,D} = 0.5 \ll J_{L,L} = J_{D,D} = 25 = T_L = T_D$ and to $J_{L,D} = 25 = T_L = T_D \gg J_{L,L} = J_{D,D} = 0.5$, respectively.

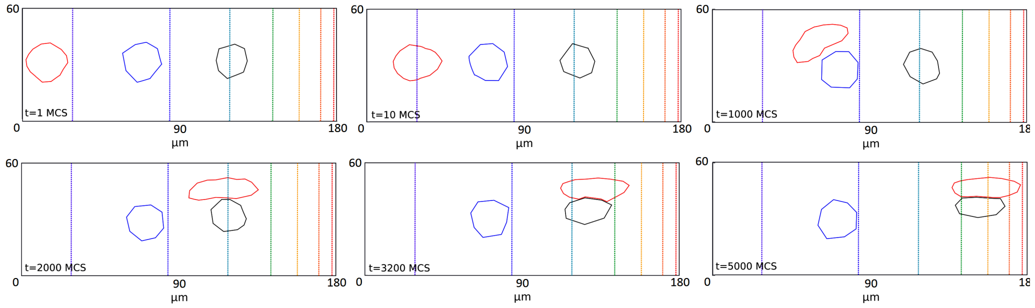

Figure 5: Test simulation of cell dynamics upon chemotactic stimulation. Three cells are aligned along the horizontal direction. The left individual is the only one sensitive to the chemical substance, whose source is extended along the entire right border of the domain. The left and the right cells are of the same type (say, epithelial) and therefore strongly adhere. The cell in the middle is of another type (say, endothelial). The parameter setting is given in the text.

Algorithm		Execution Time (sec)	Relative Slowdown (%)
traditional CPM		254	-
vertex-based CPM	without cell membrane node renumbering	325	27.95
	with cell membrane node renumbering	413	62.25

(A)

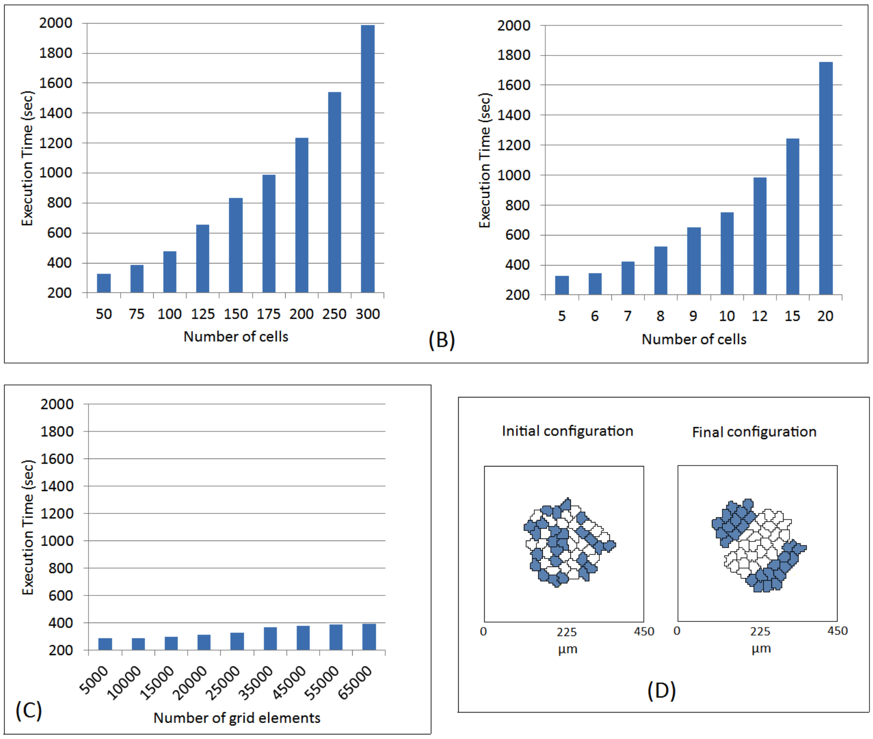

Figure 6: Analysis of the efficiency of the algorithm underlying the proposed node-based CPM. (A) Comparison of the execution time of comparable cell sorting simulations as obtained either from our method or from the traditional CPM. (B) Computational performance of our method upon variations in the number of cells or in the number of membrane nodes defining each cell. (C) Computational performance of our method upon variations in the number of the domain grid elements. (D) Initial and final (i.e., at 5000 MCS) configurations of the cell sorting simulation employed with the traditional CPM and used for comparing the algorithmic efficiency of our method. The system Hamiltonian is given in Eq. (19), whereas the model parameters are the same as in the case of Fig. 4 (bottom-right panel).